Strain phase equilibria and phase-field method of ferroelectric polydomain: A case study of monoclinic $K_xNa_{1-x}NbO_3$ thin films

Bo Wang[1,2*], Meng-Jun Zhou[3], Adriana Ladera[4,†], Long-Qing Chen[1,*]

1 Materials Research Institute and Department of Materials Science and Engineering, The Pennsylvania State University, University Park, Pennsylvania 16802, USA

2 Materials Science Division, Lawrence Livermore National Laboratory, California 94550, USA

3 State Key Laboratory of Advanced Technology for Materials Synthesis and Processing, Center of Smart Materials and Devices, School of Materials Science and Engineering, Wuhan University of Technology, No.122 Luoshi Road, Wuhan 430070, P. R. China

4 Department of Computer Science and Engineering, University of South Florida, Tampa, Florida 33620, USA

[†]5 Current address: The Center for Computational Science and Engineering, MIT, Cambridge, MA 02139, USA

Abstract

Knowledge of the thermodynamic equilibria and domain structures of ferroelectrics is critical to establishing their structure-property relationships that underpin their applications from piezoelectric devices to nonlinear optics. Here, we establish the strain condition for strain phase separation and polydomain formation and analytically predict the corresponding domain volume fractions and wall orientations of, relatively low symmetry and theoretically more challenging, monoclinic ferroelectric thin films by integrating thermodynamics of ferroelectrics, strain phase equilibria theory, microelasticity, and phase-field method. Using monoclinic $K_xNa_{1-x}NbO_3$($0.5 < x < 1.0$) thin films as a model system, we establish the polydomain strain-strain phase diagrams, from which we identify two types of monoclinic polydomain structures. The analytically predicted strain conditions of formation, domain volume fractions, and domain wall orientations for the two polydomain structures are consistent with phase-field simulations and in good agreement with experimental results in literature. The present study demonstrates a general, powerful analytical theoretical framework to predict the strain phase equilibria and domain wall orientations of

* Corresponding authors
Email addresses: wang111@llnl.edu (B. Wang), lqc3@psu.edu (L.-Q. Chen)

polydomain structures applicable to both high- and low-symmetry ferroelectrics and provide fundamental insights into the equilibrium domain structures of ferroelectric $K_xNa_{1-x}NbO_3$ thin films that are of technology relevance for lead-free dielectric and piezoelectric applications.

1. Introduction

The physical responses of ferroelectric materials to external thermal, mechanical, electric, magnetic and optical stimuli depend not only on the intrinsic crystal structure but also on the spatial configuration of ferroelectric domains and their interfaces known as the domain walls. It is of critical importance to understand the formation conditions and equilibrium structures of specific ferroelectric domains and domain walls in order to effectively tune the macroscopic performance of ferroelectric ceramics, bulk single crystals, epitaxial thin films, and nanostructures for various applications such as high-power dielectric capacitors(1), piezoelectric transducers(2), non-volatile memories(3), and nonlinear optical devices(4).

The domain structures of many ferroelectric materials can be considered as an assembly of basic building blocks known as polydomains. A polydomain consists of a pair of domain variants alternating in space with a well-defined domain wall plane. Understanding the polydomain structure is fundamental to the theoretical and experimental studies of more complex, hierarchical domain structures. Typical polydomain of tetragonal and rhombohedral ferroelectric thin films are schematically shown in Figure 1a and b, respectively. The low-energy, permissible domain walls of these polydomain structures are usually parallel to the low-index planes such as $\{100\}_{pc}$ and $\{110\}_{pc}$ identical to their bulk counterparts, and they have been extensively studied from experiments and theories (5,6). However, for orthorhombic ferroelectrics, such as $KNbO_3$, the permissible domain walls typically do not coincide with low-index planes but depends on the

spontaneous strain difference of adjacent domain variants, which is known as the S-walls where S stands for *strange*(7). Moreover, for thin films on a substrate, the lattice mismatch between a film and substrate can further distort the orthorhombic phase into monoclinic symmetry, resulting in more interesting behavior such as tunable domain walls by varying the chemical composition (8). The structural features of polydomain structures in these low-symmetry ferroelectric thin films have been much less studied compared with their tetragonal and rhombohedral counterparts, which might be attributed to the unavailability of high-quality epitaxial thin films, requirements of advanced characterization techniques to distinguish the low-symmetry phases, and necessity for more complicated theoretical analyses.

The recent advances in the epitaxial growth of high-quality, single-crystalline KNN thin films have enabled the exploration of ferroelectric phases in these films with various chemical compositions and thickness, subject to different misfit strains and temperatures (8–18). Many ferroelectric phases have been identified by advanced X-ray diffractions, including orthorhombic *c*-phase (13), orthorhombic a_1/a_2-phase(14,16), monoclinic a_1a_2-phase(8,11,15), monoclinic M_C-phase(9,10,12,13,19), and monoclinic M_A-phase (9,10,20). Meanwhile, polydomain structures of different phases have been directly observed in real space using piezoresponse force microscopy. For the M_C-phase, stripe-like polydomains consisting of two ferroelastic domain variants are observed(12,13), which we call a_1c/a_2c polydomains. Another type of polydomain structure resembles a herringbone-like pattern, consisting of one domain variant of the M_C-phase and one variant of the a_1a_2-phase (15), and we lable them a_1a_2/M_C polydomains. Combination of different variants of the polydomains forms hierarchical, superdomain structures(12,15). The domain wall orientations of the a_1c/a_2c and a_1a_2/M_C polydomain structures have also been analysed previously (8,12). In both cases, the domain walls are not parallel to any low-index planes. If we define the

domain wall inclination angles, ξ and ψ, with respect to the in-plane and out-of-plane directions, respectively, as shown in Figure 1, the experiments show that $\xi = 45°$ and $\psi = 19\pm3°$ for the a_1c/a_2c polydomain structure of $K_{0.7}Na_{0.3}NbO_3$ thin films grown on $TbScO_3$ (12) while $\psi = 45°$ and ξ varies from 24° to 41° for $K_xNa_{1-x}NbO_3$ ($0.8 \leq x \leq 0.95$) grown on $NdScO_3$ depending on the composition x(8). These results, however, have not been systematically investigated theoretically.

There have been several theoretical studies on the KNN epitaxial thin films (21–24). The temperature-misfit strain phase diagrams of the KNN thin films are established using the Landau-Ginsburg-Devonshire (LGD) model (23) and phase-field simulations(21,24). The traditional LGD method often assumes either monodomain state or specific domain wall orientations, whereas the phase-field method, though free of *a priori* assumption on the domain structures, is computationally expensive. The recently developed strain phase equilibrium theory (25) offers a powerful yet efficient approach to determine the polydomain phase diagrams without assumption on the specific domain structures and has been successfully employed to study the multiphase/multidomain stability in $BiFeO_3$ (26), $PbTiO_3$ (25) and other non-perovskite oxides(27). Nevertheless, its application to monoclinic ferroelectrics has not yet been explored.

For the theoretical prediction of domain wall orientations, despite a few studies focusing on monoclinic ferroelectric bulk crystals using the mechanical compatibility condition (28,29), this geometry-based method is limited to permissible domain walls where there is no lattice mismatch in the domain wall plane and thus no elastic energy is generated(7,30,31). However, for polydomains in biaxially strained thin films, the mechanical compatibility condition is not completely satisfied in general because of the misfit strains may result in nonequivalent spontaneous strains of the domain variants. Therefore, it requires a more general energy-based

approach to predict the low-energy domain wall orientations for polydomain structures in ferroelectric thin films (32–35).

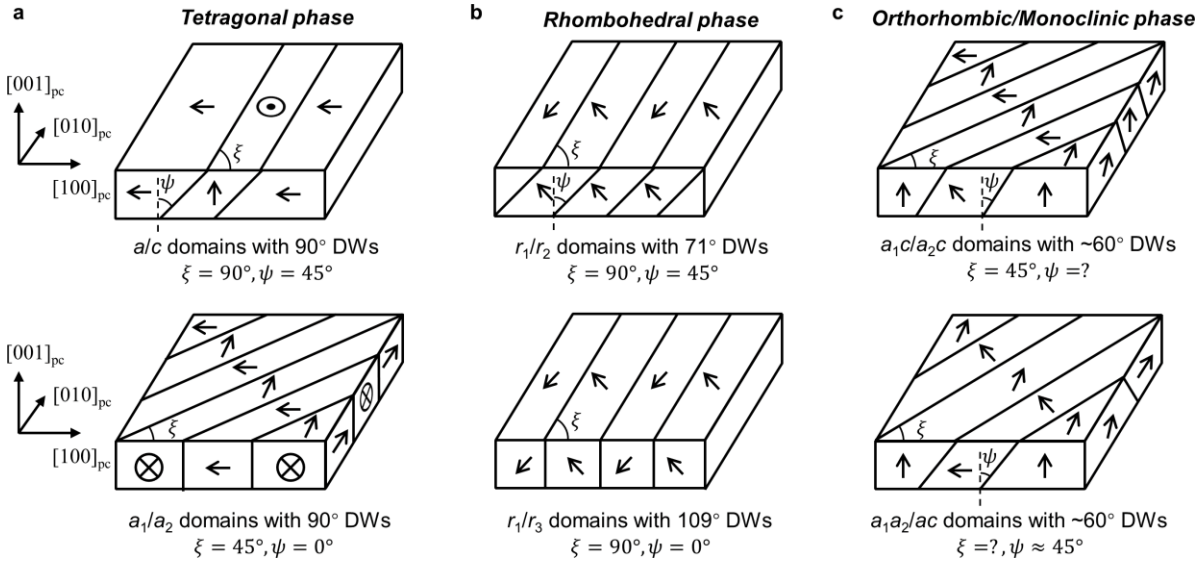

Figure 1 Schematics of typical polydomain structures of $(001)_{pc}$-oriented ferroelectric thin films with different lattice symmetries. (a) The a/c and a_1/a_2 polydomain of tetragonal phase. (b) The r_1/r_2 and r_1/r_3 polydomains of rhombohedral phase. (c) The a_1c/a_2c and a_1a_2/M_C polydomains of the orthorhombic/monoclinic phase. The black arrows in each domain variant indicate the direction of the polarization vector projected onto the plane. The domain wall inclination angles ψ and ξ are labeled.

The present work aims to demonstrate a general theoretical framework to predict the strain equilibrium conditions, domain volume fractions, and wall orientations of polydomain structures of low-symmetry ferroelectrics. We take a $(001)_{pc}$-oriented KNN epitaxial thin film as a model system and predict the two representative polydomain structures of monoclinic ferroelectric phase (i.e., a_1c/a_2c and a_1a_2/M_C polydomain) using a combination of LGD theory, strain phase equilibrium theory, microelasticity, and phase-field simulations. We construct the strain-strain phase diagrams of KNN using the LGD theory and strain phase equilibrium theory to reveal the

strain conditions for the formation of the two polydomain structures. We determine the volume fractions of the coexisting domain variants from a geometric lever-rule construction. We predict the energy-favored domain wall orientations using the microelasticity theory with the strain states of individual domain variants informed from the strain phase diagram. Further, we perform phase-field simulations to verify the theoretical predictions and compare them with experiments in literature. We also discuss four critical factors affecting the accurate prediction of the domain wall orientations.

The rest of the article is organized as follows. In Section 2, we will first state the conventions, notations, and definitions adopted throughout the work to avoid ambiguity. Then, we describe the LGD model of ferroelectrics, the strain phase equilibrium theory, the microelasticity theory for predicting the low-energy domain wall orientations, and the phase-field model of ferroelectric thin films. In Section 3, we present the main results of our theoretical predictions including the polydomain strain-strain phase diagrams of KNN thin films, volume fractions of coexisting domains, and domain wall orientations and compare them with our phase-field simulation results and existing experimental measurements in literature. In Section 4, we discuss four influencing factors that affect the accurate determination of domain wall orientations of the polydomain structures. We summarize our findings and remark on open questions in Section 5.

2. Methods

2.1 Convention, notation, and definitions

We define the Miller indices denoting the lattice planes and directions either in the pseudocubic coordinate system (with *pc* in the subscript, e.g., $(110)_{pc}$) or in the orthorhombic phase of the scandate substrates (with O in the subscript, e.g., $(110)_O$). Care needs to be taken on the different definitions of the pseudocubic lattice constants for the orthogonal scandate substrates and the

perovskite oxide thin films (36). This is critical in correctly determining the misfit strains of biaxially KNN thin films. All the results in the present work are obtained for $(001)_{pc}$-oriented KNN thin films on $(001)_{pc}$-oriented $SrTiO_3$ or $(110)_O$-oriented scandate substrates. Nevertheless, the theoretical approach is applicable to ferroelectric thin films and substrates with arbitrary orientations.

Second, we label different ferroelectric phases and their corresponding spontaneous polarization as follows(37): a_1-phase ($|P_1| \neq 0$, $|P_2| = 0$, $|P_3| = 0$), a_2-phase ($|P_1| = 0$, $|P_2| \neq 0$, $|P_3| = 0$), c-phase ($|P_1| = 0$, $|P_2| = 0$, $|P_3| \neq 0$), a_1c-phase ($|P_1| \neq 0$, $|P_2| = 0$, $|P_3| \neq 0$), a_2c-phase ($|P_1| = 0$, $|P_2| \neq 0$, $|P_3| \neq 0$), a_1a_2-phase ($|P_1| \neq 0$, $|P_2| \neq 0$, $|P_3| = 0$), and r-phase ($|P_1| \neq 0$, $|P_2| \neq 0$, $|P_3| \neq 0$). Following Ref. (17), by M_C-phase we refer to either the a_1c- or a_2c-phases, despite a_1a_2-phase also exhibits the M_C symmetry when $|P_1| \neq |P_2|$. We do not distinguish the orthorhombic phases as special cases of the a_1c-, a_2c-, and a_1a_2-phases when the two nonzero polarization components become identical in magnitude (e.g., $|P_1| = |P_2| \neq 0$, $|P_3| = 0$). Instead, we refer to all of them as the monoclinic phase. The M_A-phase can be considered as a special case of the r-phase where $|P_3|>|P_1|=|P_2| \neq 0$ or $|P_1|>|P_2|=|P_3| \neq 0$ or $|P_2|>|P_1|=|P_3| \neq 0$, while the M_B-phase can be considered as a special case of the r-phase where $|P_3|<|P_1|=|P_2| \neq 0$ or $|P_1|<|P_2|=|P_3| \neq 0$ or $|P_2|<|P_1|=|P_3| \neq 0$. Also note that the a_1-, a_2-, and c-phases, while having uniaxial ferroelectric polarization, may have unequal pseudocubic lattice constants ($a \neq b \neq c$) in general and thus are referred as the orthorhombic phase in this work, following Ref. (16). Each phase consists of several ferroelectric domain variants. For example, a_1c-phase consists of $a_1^+c^+$, $a_1^+c^-$, $a_1^-c^+$, $a_1^-c^-$ domain variants where the $\pm$ in the superscript corresponds to the sign of the polarization components. For example, the $a_1^+c^+$-domain has polarization $P_1 > 0$, $P_2 = 0$, $P_3 > 0$. Additionally, we use the term *phase* and *domain* loosely. For

example, the a_1c-, a_2c-, and a_1a_2-phases can be regarded as three ferroelastic domain variants of the M_C-phase.

Third, in principle, a domain wall refers to an interface separating two domain variants of the same phase with the same crystallographic symmetry, whereas an interphase boundary refers to an interface separating two phases with different symmetries. In this sense, as will be seen in Section 3.2.2, the interface of the a_1a_2/M_C-type polydomain should be an interphase boundary. To avoid complexity in the terminology, we do not distinguish domain walls and interphase boundaries but refer to both of them as domain walls in the rest of this work. By polydomain we mean any periodic structure consisting of a pair of alternating domain variants that may or may not have the same symmetry. If the neighboring domains of a polydomain structure become identical by a mirror-symmetry operation with respect to the domain wall plane, we call the polydomain a polytwin. In this sense, the a_1c/a_2c-type polydomain is also polytwin, whereas the a_1a_2/M_C-type polydomain is not in general, as will be seen in Section 3.2. In this work, we use polydomain to refer to polytwin as well.

Finally, we employ the Einstein summation in all equations throughout this work unless otherwise stated.

2.2 Landau-Ginzburgh-Devonshire theory of ferroelectric transitions

The Landau-Ginzburg-Devonshire theory has been successfully applied to describe the paraelectric-ferroelectric and ferroelectric-ferroelectric phase transitions in perovskite oxides. For proper ferroelectrics, the spontaneous polarization $\boldsymbol{P}$ is the primary order parameter, and the corresponding Landau-type free energy density of a homogeneous monodomain ferroelectric can be written as

$$f = \alpha_{ij}P_iP_j + \alpha_{ijkl}P_iP_jP_kP_l + \alpha_{ijklmn}P_iP_jP_kP_lP_mP_n + \alpha_{ijklmnop}P_iP_jP_kP_lP_mP_nP_oP_p$$
$$+\frac{1}{2}c_{ijkl}\left(\varepsilon_{ij} - \varepsilon_{ij}^0\right)\left(\varepsilon_{ij} - \varepsilon_{ij}^0\right) - \frac{1}{2}\kappa_{ij}E_iE_j - P_iE_j \quad (1)$$

where the α's are the Landau coefficients under the stress-free condition, c_{ijkl} is the elastic compliance of the parent phase under zero-electric field condition, κ_{ij} is the background dielectric permittivity under the zero stress condition, ε_{ij} is the total strain, ε_{ij}^0 is the spontaneous strain calculated as $\varepsilon_{ij}^0 = Q_{ijkl}P_kP_l$ where Q_{ijkl} is the electrostrictive coefficient. For the thermodynamic analysis in this work, we assume the depolarization field is completely eliminated by the short-circuit electric boundary condition, and no applied electric field.

For ferroelectric thin films subject to biaxial strains, the components of the total strain ε_i (i = 1-6, in Voigt notation) can be solved by the conditions,

$$\varepsilon_1 = \varepsilon_{xx}^m, \varepsilon_2 = \varepsilon_{yy}^m, \frac{\partial f}{\partial \varepsilon_3} = 0, \frac{\partial f}{\partial \varepsilon_4} = 0, \frac{\partial f}{\partial \varepsilon_5} = 0, \frac{\partial f}{\partial \varepsilon_6} = 0. \quad (2)$$

The misfit strains, ε_{xx}^m and ε_{yy}^m , are defined as $\varepsilon_{xx}^m = \frac{a_s - a_f}{a_f}$ and $\varepsilon_{xx}^m = \frac{b_s - a_f}{a_f}$ where a_s and b_s are the pseudocubic lattice constants of the substrate while a_f the pseudocubic lattice constant of the ferroelectric film. Notably, in solving Equation (2), we assume $\frac{\partial f}{\partial \varepsilon_6} = 0$ rather than the commonly used condition $\varepsilon_6 = 0$ to accommodate the nonzero shear component of the spontaneous strain of monodomain a_1a_2 domains, i.e., $\varepsilon_6^0 = Q_{44}P_1P_2$. The physical significance of this replacement is to assume that the thin film tends to spontaneously form equal amounts of $a_1^+a_2^+$ and $a_1^-a_2^+$ domain variants with opposite spontaneous shear strains, so that $\varepsilon_6^{0,a_1^+a_2^+} + \varepsilon_6^{0,a_1^-a_2^+} = 0$, to accommodate the zero shear strain constraint imposed by the substrate and thus relax the elastic strain energy.

By plugging the solution of Equation (2) into (1) we arrive at an expression of f in terms of P_i for a given set of ε_{xx}^m and ε_{yy}^m. The polarization at equilibrium P_i^{eq} for a given domain state can be obtained by minimizing f with respect to P_i, i.e.,

$$\frac{\partial f}{\partial P_i} = 0, \frac{\partial^2 f}{\partial P_i^2} > 0, i = 1,2,3, \tag{3}$$

subject to specific constraints on the polarization components. For example, for a_1c domain, Equation (3) is solved with the constraints $P_1 \neq 0$, $P_2 = 0$ and $P_3 \neq 0$. The solution of (3) is then plugged into Equation (1) to obtain the equilibrium free energy $f_{\mathrm{eq}} = f|_{\boldsymbol{P}=\boldsymbol{P}^{\mathrm{eq}}}$.

Following this procedure, we obtained $P_i^{\mathrm{eq}}(\varepsilon_{xx}^m, \varepsilon_{yy}^m)$ and $f_{\mathrm{eq}}(\varepsilon_{xx}^m, \varepsilon_{yy}^m)$ for the three monoclinic phases (a_1c-, a_2c-, and a_1a_2-phases), three orthorhombic phases (a_1-, a_2-, and c-phases), and one triclinic phase (r-phase) of KNN thin films of different compositions at room temperature. Notice that the expressions in Equation (1) can be greatly simplified by considering the cubic symmetry of the paraelectric phase of KNN. Nevertheless, the closed-form of $P_i^{\mathrm{eq}}(\varepsilon_{xx}^m, \varepsilon_{yy}^m)$ and $f_{\mathrm{eq}}(\varepsilon_{xx}^m, \varepsilon_{yy}^m)$ is not always guaranteed, thereby numerical solution is adopted in the present work. All parameters for the LGD model of KNN are listed in Table II as adopted from Ref. (24,38). These parameters are also adopted in the phase-field model in Section 2.5. In the rest of the work, we will drop the superscript "eq" in P_i^{eq}, and by P_i we will always refer to the spontaneous polarization at equilibrium.

2.3 Strain phase equilibrium theory

We apply the strain phase equilibrium theory to establish the strain-strain phase diagrams of KNN thin films. The calculation procedure is briefly outlined below while the detailed derivation can be found in Ref. (27). From the LGD theory of monodomain ferroelectrics described in Section 2.2,

we can obtain the equilibrium free energy density of different phases α in terms of the misfit strains ε_{xx}^m and ε_{yy}^m, i.e., $f_{\mathrm{eq}}^{\alpha}\left(\varepsilon_{xx}^m, \varepsilon_{yy}^m\right)$. For phase $\alpha \in \{a_1a_2, a_1c, a_2c, a_1, a_2, c, r\}$. With the incoherent interface assumption, the elastic interaction between neighboring strain domains/phases can be neglected, and the orientation of the interphase boundary/domain wall does not need to be assumed *a priori*. In this case, the free energy density of the phase/domain mixture can be written as a summation of the individual phases/domains weighted by their volume fractions, and the equilibrium is obtained by minimizing the total free energy with respect to the volume fractions and strains of individual domains/phases. Geometrically, these conditions for strain phase/domain coexistence can be determined by the generalized common tangent construction with respect to the strain components, allowing for efficient establishment of high-dimensional strain phase diagrams (27). Following this method, we construct the strain-strain phase diagram by determining the phase-coexistence between any two or three phases based on the common tangent construction. For two-phase equilibria with the two phases denoted as α and β, the conditions for phase coexistence are written as

$$\left.\frac{\partial f_{\mathrm{eq}}^{\alpha}}{\partial \varepsilon_{xx}^m}\right|_{\substack{\varepsilon_{xx}^m=\varepsilon_1^{\alpha} \\ \varepsilon_{yy}^m=\varepsilon_2^{\alpha}}} = \left.\frac{\partial f_{\mathrm{eq}}^{\beta}}{\partial \varepsilon_{xx}^m}\right|_{\substack{\varepsilon_{xx}^m=\varepsilon_1^{\beta} \\ \varepsilon_{yy}^m=\varepsilon_2^{\beta}}} = \sigma_1, \tag{4a}$$

$$\left.\frac{\partial f_{\mathrm{eq}}^{\alpha}}{\partial \varepsilon_2^m}\right|_{\substack{\varepsilon_{xx}^m=\varepsilon_1^{\alpha} \\ \varepsilon_{yy}^m=\varepsilon_2^{\alpha}}} = \left.\frac{\partial f_{\mathrm{eq}}^{\beta}}{\partial \varepsilon_2^m}\right|_{\substack{\varepsilon_{xx}^m=\varepsilon_1^{\beta} \\ \varepsilon_{yy}^m=\varepsilon_2^{\beta}}} = \sigma_2, \tag{4b}$$

$$f_{\mathrm{eq}}^{\alpha}(\varepsilon_1^{\alpha}, \varepsilon_2^{\alpha}) - \sigma_1\varepsilon_1^{\alpha} - \sigma_2\varepsilon_2^{\alpha} = f_{\mathrm{eq}}^{\beta}\left(\varepsilon_1^{\beta}, \varepsilon_2^{\beta}\right) - \sigma_1\varepsilon_1^{\beta} - \sigma_2\varepsilon_2^{\beta}, \tag{4c}$$

where $(\varepsilon_1^{\alpha}, \varepsilon_2^{\alpha})$ and $(\varepsilon_1^{\beta}, \varepsilon_2^{\beta})$ are the total strains for the α and β phases, respectively, and σ_1 and σ_2 are the stress at equilibrium. Note that there are six unknowns while there are only five equations in Equation (4). Therefore, the solution is not unique, and one of the unknowns should

serve as an independent parametric variable. This can be understood from the Gibbs phase rule for the strain equilibria (25), i.e., for single chemical-component ($N_c = 2$) and two strain-component system ($N_s = 2$) at a constant temperature, the degree of freedom (N_f) for two-phase coexistence ($N_p = 2$) is calculated to be $N_f = N_s + N_c - N_p = 2 + 1 - 2 = 1$. Geometrically, the two-phase region in the strain-strain phase diagram corresponds to the projection of a set of common tangent lines of the two energy surfaces onto the two-dimensional phase diagram plane, which is known as the tie-lines (27,39). The pairs of strains $(\varepsilon_1^\alpha, \varepsilon_2^\alpha)$ and $(\varepsilon_1^\beta, \varepsilon_2^\beta)$ correspond to the endpoints of the tie-lines and delineate the phase boundaries of the two-phase regions.

Likewise, for three-phase equilibria between the phase α, β and γ, the equilibrium condition can be written as

$$\left.\frac{\partial f_{\mathrm{eq}}^{\alpha}}{\partial \varepsilon_{xx}^{m}}\right|_{\substack{\varepsilon_{xx}^{m}=\varepsilon_1^{\alpha} \\ \varepsilon_{yy}^{m}=\varepsilon_2^{\alpha}}} = \left.\frac{\partial f_{\mathrm{eq}}^{\beta}}{\partial \varepsilon_{xx}^{m}}\right|_{\substack{\varepsilon_{xx}^{m}=\varepsilon_1^{\beta} \\ \varepsilon_{yy}^{m}=\varepsilon_2^{\beta}}} = \left.\frac{\partial f_{\mathrm{eq}}^{\gamma}}{\partial \varepsilon_{xx}^{m}}\right|_{\substack{\varepsilon_{xx}^{m}=\varepsilon_1^{\gamma} \\ \varepsilon_{yy}^{m}=\varepsilon_2^{\gamma}}} = \sigma_1, \tag{5a}$$

$$\left.\frac{\partial f_{\mathrm{eq}}^{\alpha}}{\partial \varepsilon_{yy}^{m}}\right|_{\substack{\varepsilon_{xx}^{m}=\varepsilon_1^{\alpha} \\ \varepsilon_{yy}^{m}=\varepsilon_2^{\alpha}}} = \left.\frac{\partial f_{\mathrm{eq}}^{\beta}}{\partial \varepsilon_{yy}^{m}}\right|_{\substack{\varepsilon_{xx}^{m}=\varepsilon_1^{\beta} \\ \varepsilon_{yy}^{m}=\varepsilon_2^{\beta}}} = \left.\frac{\partial f_{\mathrm{eq}}^{\gamma}}{\partial \varepsilon_{yy}^{m}}\right|_{\substack{\varepsilon_{xx}^{m}=\varepsilon_1^{\gamma} \\ \varepsilon_{yy}^{m}=\varepsilon_2^{\gamma}}} = \sigma_2, \tag{5b}$$

$$f_{\mathrm{eq}}^{\alpha}(\varepsilon_1^{\alpha}, \varepsilon_2^{\alpha}) - \sigma_1\varepsilon_1^{\alpha} - \sigma_2\varepsilon_2^{\alpha} = f_{\mathrm{eq}}^{\beta}\left(\varepsilon_1^{\beta}, \varepsilon_2^{\beta}\right) - \sigma_1\varepsilon_1^{\beta} - \sigma_2\varepsilon_2^{\beta} = f_{\mathrm{eq}}^{\gamma}\left(\varepsilon_1^{\gamma}, \varepsilon_2^{\gamma}\right) - \sigma_1\varepsilon_1^{\gamma} - \sigma_2\varepsilon_2^{\gamma}, \tag{5c}$$

from which the pairs of strains $(\varepsilon_1^\alpha, \varepsilon_2^\alpha)$, $(\varepsilon_1^\beta, \varepsilon_2^\beta)$, $(\varepsilon_1^\gamma, \varepsilon_2^\gamma)$ for the α, β, and γ phases, respectively, and the stress σ_1 and σ_2 at equilibrium can be obtained. Since there are eight equations and eight unknowns, the solution is unique in this case which is consistent with the Gibbs phase rule (25), i.e., $N_f = N_s + N_c - N_p = 2 + 1 - 3 = 0$. Geometrically, the three-phase equilibrium corresponds to identifying the common tangent plane of the three free energy surfaces (f_{eq}^{α}, f_{eq}^{β}, and f_{eq}^{γ}) in terms of the strain variables. The common tangent plane is bounded by three common tangent lines of

the two-phase regions, forming a common tangent triangle which is projected onto the strain-strain phase diagram to obtain the three-phase region (27). Notably, depending on the specific form of f_{eq}, there might be either no solution of Equation (5), which means the three-phase cannot coexist under the given condition, or degenerate solution where $(\varepsilon_1^{\alpha}, \varepsilon_2^{\alpha})$, $(\varepsilon_1^{\beta}, \varepsilon_2^{\beta})$, $(\varepsilon_1^{\gamma}, \varepsilon_2^{\gamma})$ become identical. In the latter case, the three phase becomes undistinguishable, i.e., the first-order phase transition becomes a second-order transition, and the solved strain state corresponds to a critical point in the strain-strain phase diagram. As will be seen in Section 3.1, this scenario occurs when two monoclinic phases (i.e., a_1c-, a_2c-, and a_1a_2-phases) transition into one orthorhombic phase (i.e., a_1, a_2, and c-phases) as the misfit strain varies. The phase boundary for the second-order transition is indicated by equating f_{eq} of the adjacent phases and represented by dashed curves in the phase diagrams (c.f. Figure. 2). Also note that, according to our calculation, the r-phase does not become stable phase in the ranges of misfit strains ($-2.0\% \leq \varepsilon_{xx}^{m} \leq 2.5\%$ and $-2.0\% \leq \varepsilon_{yy}^{m} \leq 2.5\%$), temperature ($T$ = 300K) and composition (x = 0.5 ~ 1.0) considered in this work.

2.4 Microelasticity theory for predicting low-energy domain wall orientations

Permissible domain walls satisfying the mechanical compatibility condition along the domain wall plane for all ferroelectric species have been well documented (30,31). Similar compatibility conditions have been proposed to account for the charged domain walls (40) and domain walls of improper ferroelectrics(41). When the mechanical compatibility conditions are not satisfied, the optimal orientation of the domain walls should be determined by minimizing some metrics of the incompatibility(32) such as the long-range elastic energy associated with the lattice mismatch at the domain wall plane in terms of the domain wall orientation(35,42). The energy-based method can be further extended to include long-range electrostatic energy, short-range domain wall interfacial energy and surface energy associated with finite-size systems (35), allowing for a more

comprehensive thermodynamics model of polydomain structures which can be used to estimate the equilibrium domain size for a polydomain formation (34). This approach has been employed to study the domain walls and heterophase boundaries of $Pb(Zr_{1-x}Ti_x)O_3$ (33), $Ba(Zr_{0.2}Ti_{0.8})O_3$ (43), and $BiFeO_3$ thin films (34).

In this work, we assume the elastic strain energy governs the domain wall orientation and adopt the microelasticity theory (35,42) to determine the low-energy domain walls. The electrostatic compatibility condition is used to distinguish the charged neutral domain walls. According to Ref. (34), the coherent elastic strain energy associated with the formation of laminated polydomain structure consisting of alternating phase α and β can be written as $E_{\text{elas}}^{\text{coh}} = \frac{1}{2}\omega_1\omega_2 B(\boldsymbol{n})V$ where V is the volume of the system, $\boldsymbol{n}$ is the unit normal vector of the interphase boundary, and ω_1 and ω_2 are the volume fractions of the two domain variants. The quantity $B(\boldsymbol{n})$ can be expressed as:

$$B(\boldsymbol{n}) = c_{ijkl}\Delta\varepsilon_{ij}^0\Delta\varepsilon_{kl}^0 - n_i\Delta\sigma_{ij}^0\Omega_{jk}\Delta\sigma_{kl}^0 n_l, \tag{6}$$

where c_{ijkl} is the elastic stiffness, $\Delta\varepsilon_{ij}^0$ is the difference between the spontaneous strains of the two phases, $\Delta\sigma_{ij}^0$ is defined as $\sigma_{ij}^0 = c_{ijkl}\Delta\varepsilon_{kl}^0$, and Ω_{ij} is a second-rank tensor whose inverse is defined as $\Omega_{ij}^{-1} = c_{jklm}n_k n_l$. For ferroelectric phases α and β described by Equation (1), $\Delta\varepsilon_{ij}^0 = Q_{ijkl}P_k^\alpha P_l^\alpha - Q_{ijkl}P_k^\beta P_l^\beta$. We also assume that c_{ijkl} is identical for the two phases and homogeneous for the polydomain structure. In this sense, we can determine the energy-favored domain wall orientation by minimizing Equation (6) with respect to $\boldsymbol{n}$. Notably, for permissible domain walls, the solution of $\boldsymbol{n}$ reduces to the result based on the mechanical compatibility analysis.

The minimization of Equation (6) generally results in two solutions of $\boldsymbol{n}$ that are orthogonal to each other (42). To determine which one is the optimal domain wall plane for two ferroelectric

domain variants, we also need to consider the electrostatic energy associated with the domain wall, which can be defined as $E_{\text{elec}}^{\square} = \frac{1}{2}\omega_1\omega_2 Q(\boldsymbol{n})V$. The quantity $Q(\boldsymbol{n})$ is written as,

$$Q(\boldsymbol{n}) = \frac{(\Delta P_i n_i)^2}{\kappa_{ij} n_i n_j}, \tag{7}$$

where $\Delta \boldsymbol{P} = \boldsymbol{P}^{\alpha} - \boldsymbol{P}^{\beta}$ and $\boldsymbol{P}^{\alpha}$ and $\boldsymbol{P}^{\beta}$ are the spontaneous polarization of the two adjacent domains and κ_{ij} the dielectric permittivity. When κ_{ij} is assumed to be isotropic, as adopted in this work, the minimization of Equation (7) can be simplified into the minimization of the bound charge ρ_b^{DW} defined as,

$$\rho_b^{\text{DW}}(\boldsymbol{n}) = \Delta P_i n_i. \tag{8}$$

Since we assume the elastic energy $E_{\text{elas}}^{\text{coh}}$ is the dominant factor determining the domain wall orientation, we minimize Equations (6) and (8) sequentially to determine to identify the low-energy domain walls. Notably, if the long-range electrostatic field $E_{\text{elec}}^{\square}$ is comparable to or more pronounced than $E_{\text{elas}}^{\text{coh}}$ and thus cannot be ignored, such as for the case of strongly charged domain walls, the domain wall orientation should be determined by minimizing the summation of Equations (6) and (7) together.

2.5 Phase-field method

The phase-field method of ferroelectric materials has been well established and successfully applied to understanding the formation and evolution of domain structures in ferroelectric thin films and nanostructures (44,45). It can be regarded as an extension of the LGD model of homogeneous ferroelectrics described in Section 2.2 to inhomogeneous ferroelectrics while considering the polarization evolution. To obtain the equilibrium states, we employ the time-dependent Ginzburg-Landau (TDGL) equation to describe the evolution kinetics, i.e.,

$$\frac{\partial P_i}{\partial t} = -L_{ij}\frac{\delta F}{\delta P_j}, \tag{9}$$

where L is the kinetic coefficient and is assumed to be a constant scalar in this work. The total free energy F can be written into several terms, i.e.,

$$F = \int_V \left(f_{\text{bulk}} + f_{\text{elas}} + f_{\text{elec}} + f_{\text{grad}}\right) dv. \tag{10}$$

When built upon the LGD theory of ferroelectrics, the combination of bulk, elastic, and electric energy densities of the phase-field model, i.e., $f_{\text{bulk}} + f_{\text{elas}} + f_{\text{elec}}$ term in Equation (1), has the similar form as Equation (1) except that the uniform polarization $\boldsymbol{P}$ in (1) is replaced by the field variable $\boldsymbol{P}(\boldsymbol{x})$. The gradient energy density is written as

$$f_{\text{grad}} = \frac{1}{2} g_{ijkl}\frac{\partial P_i}{\partial x_j}\frac{\partial P_k}{\partial x_l}, \tag{11}$$

where g_{ijkl} is the gradient energy coefficient. Notably, for homogeneous ferroelectrics, f_{grad} is zero. For thermodynamic models of polydomain structures at equilibrium, it can be equal to half of the domain wall energy, i.e., $f_{\text{grad}} \sim \gamma N$ where γ is the domain wall energy density with the unit J/m^2 and N the domain wall density with the unit 1/m. In the polydomain model used for the strain energy equilibrium theory in Section 2.3, we ignore the domain energy.

We performed three-dimensional phase-field simulations to obtain the equilibrium polydomain structures of KNN thin films. The system is uniformly discretized into $128\Delta x \times 128\Delta y \times 36\Delta z$ voxels where the voxel size $\Delta x = \Delta y = \Delta z = 1$ nm. The periodic boundary condition is imposed along the x and y directions for the elastostatic and electrostatic equilibrium equations and the TDGL equation for polarization evolution. The superposition method is adopted to handle the non-periodic boundary condition along the z direction(46,47). The substrate layer with a thickness of $12\Delta z$ is used to accommodate the mechanical displacement relaxation in the substrate(46), along

with a film layer with a thickness of $20\Delta z$ and a buffer layer of the vacuum. The traction-free boundary conditions ($\boldsymbol{\sigma} \cdot \boldsymbol{n} = 0$) on the film top surface and zero-displacement condition ($\boldsymbol{u} = 0$) at the substrate bottom are adopted for solving the elastostatic equilibrium equation. The short-circuit boundary condition ($\phi = 0$) is imposed on both the top and bottom surfaces of the film layer for solving the electrostatic equilibrium equation. The natural boundary condition is assumed for the Equation 9 by truncating the polarization field at both surfaces of the film. Note that the electrostatic energy density is considered in our phase-field simulations but is ignored in the theoretical methods in Section 2.2 and 2.3. Nevertheless, it turns out to be negligible compared to the elastic energy because of the short-circuit boundary condition used in the simulations.

The parameters used for the phase-field model of KNN are the same as those in Table 1. The additional gradient energy coefficient for the phase-field model is assumed to be isotropic ($g_{11} = -g_{12} = g_{44} = 0.64\times10^{-11}$ N·m^4/C^2) and independent of composition, which gives a domain wall thickness of 0.8 nm for a 180-degree domain wall in the bulk orthorhombic phase of $K_{0.5}Na_{0.5}NbO_3$ at room temperature. The relative background dielectric permittivity κ_{ij} of the cubic phase is assumed isotropic with a value of $50\epsilon_0$ where ϵ_0 is the vacuum permittivity. Notably, the shear component of the electrostrictive tensor, i.e., Q_{44} in the Voigt notation, of $K_{0.5}Na_{0.5}NbO_3$ shows significant discrepancy in the literature, ranging from 0.029 (24) to 0.084 m^4/C^2 (23). Here, we assume that Q_{44} value is independent of the composition of KNN and equal to that of $KNbO_3$ (48), i.e., $Q_{44} = 0.052$ m^4/C^2 for all composition of KNN studied in this work. We will show in Section 3.3.3 that the choice of Q_{44} affects the equilibrium domain wall orientations for the polydomain structures of KNN thin films, and a careful comparison with experimental measurements in literature suggest that $Q_{44} = 0.029$ m^4/C^2 for $K_{0.5}Na_{0.5}NbO_3$ is the best estimation among others.

The initial state of our phase-field simulations is different from many previous works. Instead of starting from a random noise distribution as the initial state, we preset a polydomain structure consisting of two periodically alternating domain variants of equal volume fractions and presume the domain wall plane orients toward a low-index direction. This treatment is made to obtain regular polydomain structure with controlled domain variants for better comparison with the predictions based on the analytical or semi-analytical thermodynamic calculations. Specifically, we consider the polydomain formed by the $a_1^+c^+$and $a_2^+c^+$ domain variants as a representative case of the a_1c/a_2c polydomain with $(110)_{pc}$ as the initial guess of the domain wall plane, and the $a_1^+a_2^+$and $a_2^+c^+$ domain variants as a representative case of the a_1a_2/M_C polydomain with $(120)_{pc}$ as the initial guess of the domain wall plane. Notably, the periodic boundary conditions imposed along the in-plane directions of the simulations may restrict the relaxation of domain walls. This issue can be resolved by considering a pair of domain bundles as will be discussed in Section 3.3.4.

3. Results

3.1 Strain equilibria phase diagrams

Following the method described in Section 2.3, we established the misfit strain–misfit strain multidomain/multiphase diagrams of $K_xNa_{1-x}NbO_3$ at T = 300 K for compositions x = 0.5, 0.7, and 0.9, as shown in Figure 2. The three phase diagrams are similar in topology, suggesting a minor composition dependence of the phase stability in the range studied (x = 0.5 ~ 1.0), in consistent with the temperature-composition phase diagrams of KNN ceramics (38) and the temperature-misfit strain phase diagrams of KNN thin films (24). Without loss of generality, we use Figure 2a for $K_{0.7}Na_{0.3}NbO_3$ as an example to examine the main features of the phase diagrams. The misfit strain–misfit strain phase diagram consists of six single-phase regions, three two-phase regions, and one three-phase region. The phase regions are symmetric with respect to the diagonal of the

phase diagram, suggesting that the a_1c-phase and a_2c-phase are equivalent by symmetry. The transitions among the three monoclinic phases (i.e., a_1c-, a_2c- and a_1a_2-phases) are first order characterized by two-phase regions, whereas the transitions between the monoclinic and orthorhombic phases (i.e., a_1-, a_2- and c-phases) are continuous. According to the Gibbs phase rule, for a phase diagram with densities as independent variables (such as the strain components), the number of maximal coexisting phases in the phase region should either increase or decrease by one when crossing the phase boundary of first-order phase transitions (solid lines in Figure 2a) or remain unchanged when crossing the phase boundary of a continuous phase transition (dashed lines in Figure 2a). These requirements can be easily verified in all the phase regions in Figure 2, suggesting the consistency of the present results with the fundamental laws of thermodynamics.

The strain-strain phase diagrams in Figure 2 provide the strain equilibrium conditions for multi-phase coexistence in strained KNN at the room temperature. We can verify these predictions by comparing them with existing experimental datapoints (8,13,17). To this end, we calculated the misfit strains associated with various combinations of film-substrate pairs by using the pseudocubic lattice constants of bulk KNN (interpolated by assuming a Vegard's law between $KNbO_3$(49) and $K_{0.5}Na_{0.5}NbO_3$(50,51)) and substrate materials (including $SrTiO_3$ (STO), $DyScO_3$ (DSO) $GdScO_3$(GSO), $TbScO_3$(TSO), $SmScO_3$(SSO), and $NdScO_3$(NSO))(52–54). We tabulated the calculated anisotropic misfit strains and their averaged values ($\varepsilon_{\mathrm{avg}}^{\mathrm{m}} = \frac{1}{2}(\varepsilon_{xx}^{\mathrm{m}} + \varepsilon_{yy}^{\mathrm{m}})$) in Table 2 and labeled them in the corresponding phase diagrams in Figure 2. When the misfit strains are biaxially compressive with a moderate magnitude, the a_1c/a_2c phase mixture is preferred, in agreement with KNN films (x = 0.70 ~ 0.77) grown on TSO, GSO, and SSO substrates (blue dots in Figure 2a). When both misfit strain components are highly compressive beyond the M_C- to c-phase transition point, the single c-phase is stabilized, in agreement with the observation of

$K_{0.71}Na_{0.29}NbO_3$ grown on DSO (black square in Figure 2c). For $K_{0.5}Na_{0.5}NbO_3$ thin films grown on STO, the nominal compressive misfit strain is calculated to be $\varepsilon_{xx}^{\mathrm{m}} = \varepsilon_{yy}^{\mathrm{m}} = -1.8\%$. However, considering the strain relaxation as suggested in the experiments, the effective misfit strains become $\varepsilon_{xx}^{\mathrm{m}} + \varepsilon_{yy}^{\mathrm{m}} = -0.71\%$, which corresponds to a_1c/a_2c phase mixtures in Figure 2c and also agrees with the experimental reports(10).

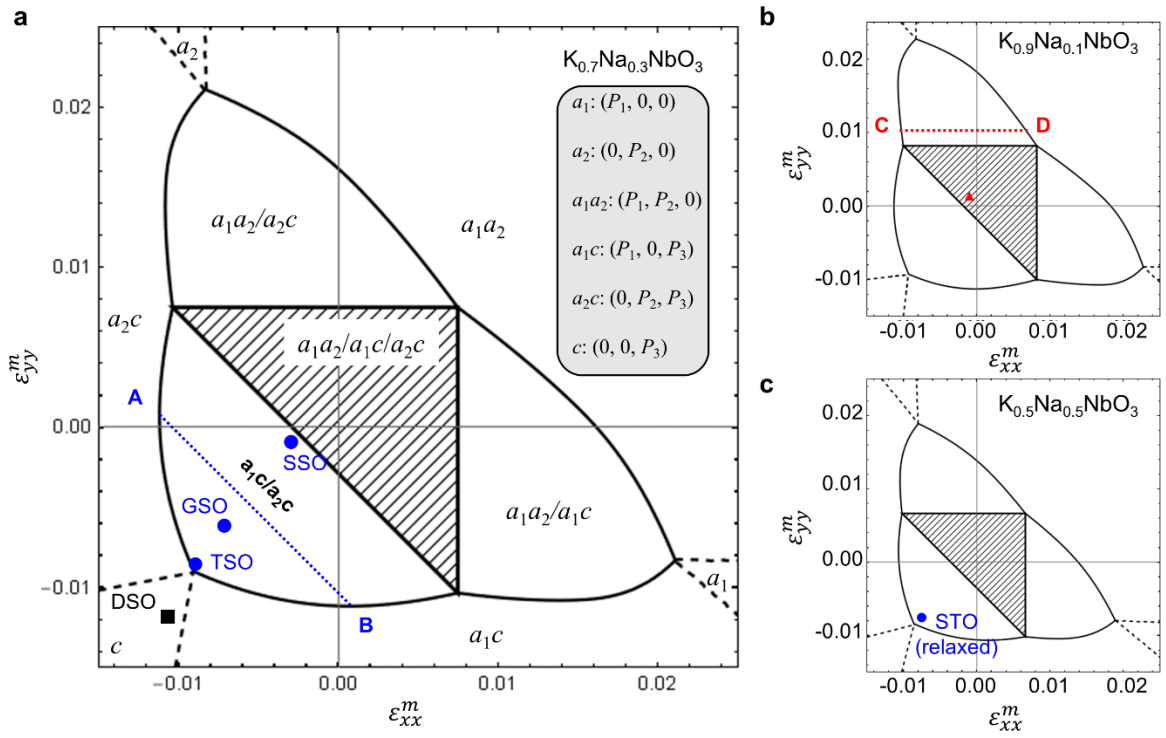

Figure 2 Multiphase/multidomain strain phase diagrams of $K_xNa_{1-x}NbO_3$ under anisotropic misfit strains at room temperature for (a) x = 0.7 (b) x = 0.9, and (c) x = 0.5. The labels of single-phase and multi-phase regions are given in (a) from which the corresponding labels in (b,c) can be deduced. The datapoints from previous experiments in literature are labeled by a red triangle (for $K_{0.7}Na_{0.3}NbO_3$ on $NdScO_3$(NSO) substrate), blue disks (for $K_{0.7}Na_{0.3}NbO_3$ on $SmScO_3$(SSO), $GdScO_3$(GSO), $TbScO_3$(TSO) substrates and $K_{0.5}Na_{0.5}NbO_3$ $SrTiO_3$(STO) substrates), and a black square (for $K_{0.9}Na_{0.1}NbO_3$ on $DyScO_3$(DSO) substrate). The phase boundaries for first-order transitions are plotted in thick solid lines and for second-order transitions are plotted in thick

dashed lines. The segment AB in dotted red and segment CD in dotted blue are used to evaluate the volume fractions of the coexisting phases by the lever rule.

When the misfit strain is highly anisotropic, e.g., being tensile and compressive respectively along two orthogonal in-plane directions, Figure 2 suggests that either the a_1a_2/a_1c or a_1a_2/a_2c phase mixture is favored. In experiments, the substrate materials that can provide the maximal anisotropic misfit strain is NSO, which results in a strain state located in the triple-phase region in Figure 2b (labeled by a red triangle). However, $K_{0.9}Na_{0.1}NbO_3$ thin films on NSO substrates reported in experiments consist of only two of the three phases, i.e., the a_1a_2-phase plus either a_1c- or a_2c-phase. In other words, while the theory predicts that a large anisotropy in the misfit strains (e.g., $\varepsilon_{yy}^{\mathrm{m}} - \varepsilon_{xx}^{\mathrm{m}} = 1.0\%$) is required to obtain the two-phase mixtures, experiments suggest it can be achieved with a moderate anisotropy ($\varepsilon_{yy}^{\mathrm{m}} - \varepsilon_{xx}^{\mathrm{m}} = 0.3\%$). There seems to be a strong bias for the in-plane polarization of the KNN films to align along the $[1\bar{1}0]_{\mathrm{O}}$ over the $[001]_{\mathrm{O}}$ direction of the NSO substrate(15). This strong in-plane asymmetry echoes back to the well-known self-poling phenomenon in the rhombohedral-like $BiFeO_3$ epitaxial thin films grown on $TbScO_3$ substrates which shows preferred 109-degree stripe domains with aligned in-plane polarization (55) and the recently discovered quasi-single-domain with preferred in-plane polarization direction in $BaTiO_3$ epitaxial thin films grown on $PrScO_3$ (56). We hypothesized that it may be attributed to the mismatch of octahedral distortions at the interface between the perovskite films and scandate substrates (56,57), which is not considered in the present model.

From the above discussion we conclude that the theoretically predicted strain equilibria of KNN thin films agree reasonably well with experimental results in literature, suggesting that the strain phase equilibrium theory is a viable method to predict the formation conditions of polydomain phase mixtures in ferroelectric thin films.

3.2 Polydomain structures

We next predict the domain wall orientation and volume fractions in the two-phase regimes shown in Figure 2. To verify the theoretical results, we compare them with our phase-field simulations and experiments in literature. To account for the misfit strain effects on the polydomain structure, we choose a series of misfit strains along the segment AB in the two-phase region of Figure 2a to study the formation of the a_1c/a_2c polydomain and the segment CD in the two-phase region of Figure 2b to study the formation of the a_1a_2/a_2c polydomain. The segment AB passes the strain state $\varepsilon_{xx}^m = -0.5\%$ and $\varepsilon_{yy}^m = -0.5\%$ and parallels with the long-edge of the shaded triangle in Figure 2a, while the segment CD passes the strain state $\varepsilon_{xx}^m = 0.0\%$ and $\varepsilon_{yy}^m = 1.0\%$ and parallels with the short-edge of the shaded triangle in Figure 2b. Note that the choice of AB and CD segments are arbitrary in the two-phase regions but needs to be the tie-lines to apply the lever rule construction. For each case, we determine the domain walls orientations by using the method described in Section 2.4 and the volume fractions of coexisting phases by using a lever rule.

3.2.1 a_1c/a_2c polydomain

The calculated domain wall plane for the a_1c/a_2c polydomain of the biaxially strained $K_{0.7}Na_{0.3}NbO_3$ is $(11k)_{pc}$ with k = 0.32, independent of the misfit strain states on AB. The corresponding domain wall inclination angles ξ = 45° and ψ = 18°. The independence of the domain wall orientation of the misfit strain can be rationalized as follows. According to the strain phase equilibrium theory neglecting the local coherency strain and domain wall energy effects due to inhomogeneity within the domains, the strain states of coexisting domains remain at the endpoints A and B for arbitrary misfit strains on the tie-line. In this sense, the equilibrium polarization and associated eigenstrains of the two domain variants remains homogeneous and constant and hence their domain wall orientations, according to Equation (6). If the misfit strain

does not vary along a tie-line, the strain states within each domain will change, which will affect the domain wall orientation at equilibrium. This scenario will be discussed in Section 3.3.1.

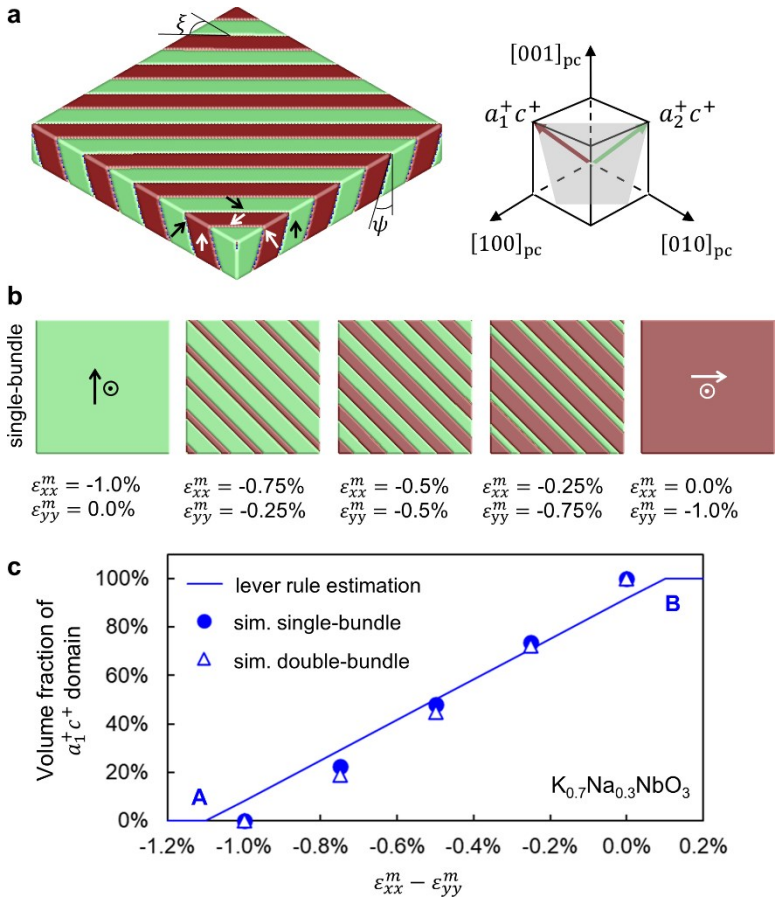

Figure 3 Phase-field simulations of a_1c/a_2c polydomain of $K_{0.7}Na_{0.3}NbO_3$ thin films at $T = 300$K. (a) The simulated domain structures at equilibrium with biaxial isotropic misfit strain $\varepsilon_{xx}^m = \varepsilon_{yy}^m = -0.5\%$. The arrows indicate the spontaneous polarization directions in each domain variant. The box on the right illustrates polarization directions of the two domain variants $a_1^+c^+$ and $a_2^+c^+$ in the pseudocubic coordinate system. (b) Top views of the polydomain structures at equilibrium subject to different misfit strains. The arrows indicate the polarization directions in each domain variant. (c) The volume fraction of $a_1^+c^+$ as a function of the anisotropy of the misfit strains measured by $\varepsilon_{xx}^m - \varepsilon_{yy}^m$.

To test the predicted domain wall orientation, we obtain the corresponding a_1c/a_2c polydomain structures by performing 3D phase-field simulations of $K_{0.7}Na_{0.3}NbO_3$ thin films subject to five different strains along segment AB. The results are summarized in Figure 3. Figure 3a shows a representative result for $\varepsilon_{xx}^m = \varepsilon_{yy}^m = -0.5\%$. We can see that domain wall plane at equilibrium is tilted away from the initial guess, $(110)_{pc}$, and the inclination angles are measured to be $\xi = 45°$ and $\psi \sim 20°$, corresponding to the $(11k)_{pc}$ plane with $k \sim 0.36$, which agrees well with the analytically predicted value ($k = 0.32$). Further, the inclination angle ψ was measured to be $19\pm3°$ for $K_{0.7}Na_{0.3}NbO_3$ thin films on TSO by high-resolution X-ray diffraction techniques (12), which also agrees quantitatively well with both the analytical and simulation values. From the cross-section views of the phase-field simulation results in Figure 3b, we also find negligible changes in the domain wall inclination angle ψ or ξ, which also agrees with analytical predictions.

We then determine the volume fractions of the a_1c- and a_2c-phases of the polydomain by applying the lever rule. Specifically, for a given point X on segment AB, the volume fraction of the a_1c-phase can be calculated as $\omega_{a_1c} = \frac{|AX|}{|AB|}$ and similar for the a_2c-phase, $\omega_{a_2c} = \frac{|XB|}{|AB|}$ where |AB| denotes the length of the segment AB. Note that $\omega_{a_1c} + \omega_{a_2c} = 1$. We compute ω_{a_1c} as a function of the anisotropy of the misfit strains defined as $\varepsilon_{xx}^m - \varepsilon_{yy}^m$ and compare the results with those from phase-field simulation in Figure 3c. It is shown that the relative volume fractions of a_1c-phase and a_2c-phases vary with the misfit strain state. This linear relation between the volume fraction and the anisotropy of the misfit strain agrees reasonably well with the phase-field simulations (dots in Figure 3c) except that the phase-coexisting region obtained from the simulations is narrower. This can be clearly seen in the simulated $a_1^+c^+/a_2^+c^+$ polydomain patterns shown in Figure 3b. Among the five misfit strain conditions considered, only three of them can stabilize the polydomain while the two endpoints relax into single-domain states. Similar differences in terms of the predicted

two-phase stability between the strain phase equilibrium theory and phase-field simulations have also been reported and discussed for tetragonal $PbTiO_3$ (25) and $BiFeO_3$ (26). It can be ascribed to the incoherent interface assumption adopted in the strain phase equilibrium theory (c.f. Section 2.3). In contrast, the coherent strain energy contribution associated with the domain walls has been fully included in the phase-field simulations. We can also draw an analogy of strain phase separation or strain spinodal to the coherent versus incoherent spinodal decomposition in chemical equilibria of binary solid solution with a miscibility gap. At a given temperature, the coherency strain energy tends to suppress phase separation.

3.2.2 a_1a_2/M$_C$ polydomain

As a second example, we study the polydomain in the a_1a_2/a_2c phase-coexisting region, which is equivalent to the a_1a_2/a_1c region by symmetry argument. The calculated domain wall orientation for the a_1a_2/a_2c polydomain of biaxially strained $K_{0.9}Na_{0.1}NbO_3$ is $(1h1)_{pc}$ with k = 0.27, independent of the misfit strain states on segment CD in Figure 2b. The corresponding domain wall inclination angles are ξ = 15° and ψ = 45°. Similar explanation applies to understanding the indifference of the domain wall orientation with respect to the misfit strain as discussed in 3.2.1. To test the analytical prediction, we obtain the polydomain structures consisting of $a_1^+a_2^+$ and $a_2^+c^+$ domain variants by performing 3D phase-field simulations of $K_{0.9}Na_{0.1}NbO_3$ thin films under a series of anisotropic misfit strains along the segment CD. The results are summarized in Figure 4. As shown in the polydomain structure for $\varepsilon_{xx}^m = 0.0\%$ and $\varepsilon_{yy}^m = 1.0\%$ (Figure 4a), the domain wall inclination angles are measured to be $\xi \sim 15°$ and $\psi \sim 45°$, corresponding to a domain wall plane $(1h1)_{pc}$ plane with $h \sim 0.27$, which agrees perfectly well with the analytical predictions. Further, the angle ξ was measured to be 15∼20° for $K_xNa_{1-x}NbO_3$ (x = 0.90 ~ 0.95) thin films on NSO (8), which agrees reasonably well with our theoretical and simulation results. The simulation

results also show the independence of the domain wall angle with respect to the misfit strain states for the polydomain structures, as shown in Figure 4b. However, one caveat is the restriction imposed by the in-plane periodic boundary conditions used in the simulations which might artificially cause the invariant domain wall plane. This issue can be avoided by considering double-bundle domain structures which is detailed in Section 3.3.4.

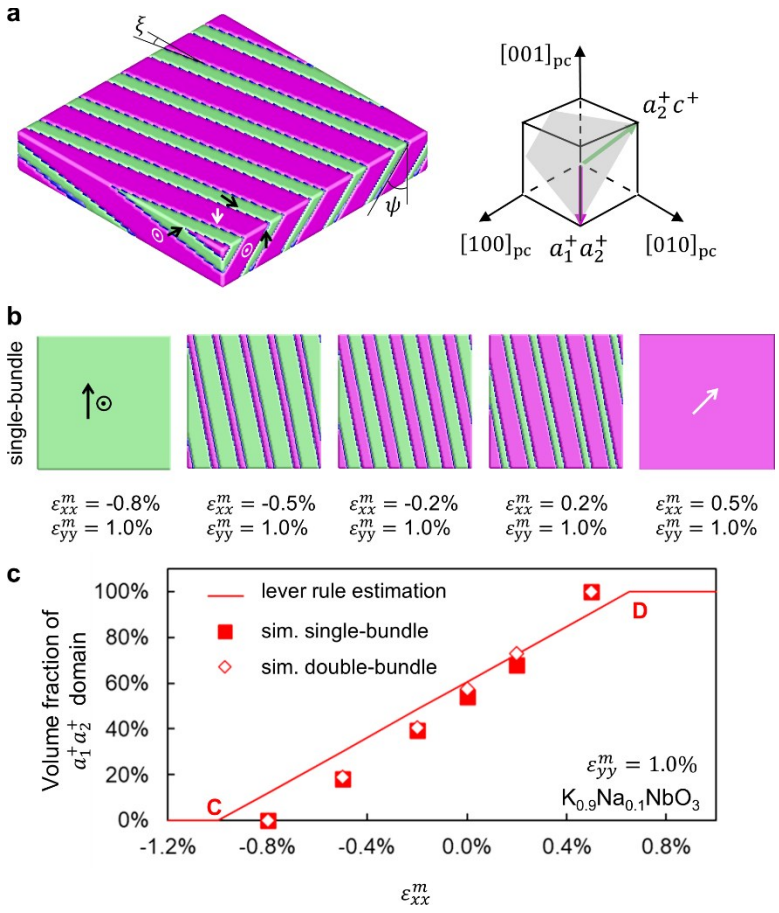

Figure 4 Phase-field simulations of a_1a_2/M$_C$ polydomain of $K_{0.9}Na_{0.1}NbO_3$ thin films at T = 300K. (a) The simulated domain structures at equilibrium with biaxial isotropic misfit strain $\varepsilon_{xx}^m = 0.0\%$ and $\varepsilon_{yy}^m = 1.0\%$. The arrows indicate the spontaneous polarization directions in each domain variant. The box on the right illustrates polarization directions of the two domain variants $a_1^+a_2^+$ and $a_2^+c^+$ in the pseudocubic coordinate system. (b) Top views of the polydomain structures at

equilibrium subject to different misfit strains. The arrows indicate the polarization directions in each domain variant. (c) The volume fraction of $a_1^+c^+$ as a function of the misfit strain component ε_{xx}^m while keeping $\varepsilon_{yy}^m = 1.0\%$.

Notably, the strain states of the a_1a_2-phase and a_2c-phase for the a_1a_2/M$_C$ polydomain are different while the strain states of the a_1c-phase and a_2c-phase are equivalent by symmetry. As a result, the domain wall for the a_1a_2/a_2c polydomain is generally impermissible walls and cannot be determined from the geometric method based on the mechanical compatibility condition(7). Notably, under certain conditions the domain wall of the a_1a_2/M$_C$ polydomain becomes permissible, i.e., when the two domain variants share the equivalent monoclinic deformation. In terms of the spontaneous polarization, this condition corresponds to the ratio $|P_2|/|P_1|$ of the a_1a_2-phase is identical to the ratio $|P_2|/|P_3|$ of the a_2c-phase (or $|P_1|/|P_3|$ of the a_1c-phase). Moreover, the angle ξ of the a_1a_2/M$_C$ polydomain will be identical to the angle ψ of the a_1c/a_2c polydomain given that the monoclinic distortions for all the domain variants are identical.

We also estimate the volume fractions of the a_1a_2- and a_2c-phases by using the lever rule similar to the case in Section 3.2.1. For a given point X along the segment CD, the volume fraction of the a_1a_2-phase is calculated as $\omega_{a_1a_2} = \frac{|\mathrm{CX}|}{|\mathrm{CD}|}$ and for the a_2c-phase, $\omega_{a_2c} = \frac{|\mathrm{XD}|}{|\mathrm{AB}|}$. Note that $\omega_{a_1a_2} + \omega_{a_2c} = 1$. We evaluate $\omega_{a_1a_2}$ as a function of the misfit strain component ε_{xx}^m along CD and compare the results with those from the phase-field simulation in Figure 4c. A reasonably good agreement is achieved between the analytical predictions and the simulation results. From the simulated $a_1^+a_2^+/a_2^+c^+$ polydomain patterns displayed in Figure 4b, we also notice that the polydomain remains stable for three of the five misfit strain conditions while the two endpoints result in single-domain states. Similar to the case of the a_1c/a_2c polydomain, this result also suggests an overestimation of the two-phase mixture regimes in the strain phase diagrams in Figure

2b due to the neglect of coherency strain energy contribution compared with the phase-field simulation results.

3.3 Factors influencing domain wall orientation

In this section, we discuss four possible factors that influence the domain wall orientation, including the misfit strain states, the choice of electrostrictive coefficient, the domain wall density, and an artificial restriction associated with the in-plane periodical boundary conditions in the phase-field simulations.

3.3.1 Effect of misfit strains

Although the examples shown above seem to suggest no misfit strain effects on the domain wall orientation for the two types of polydomain structures considered, this is true only when the misfit strains vary along the same tie-line so that the individual strain states of the coexisting domains remain unchanged. In general, there is a strong influence of the misfit strains on the low-energy domain wall plane for the two polydomain structures considered in this work, as will be shown in the following.

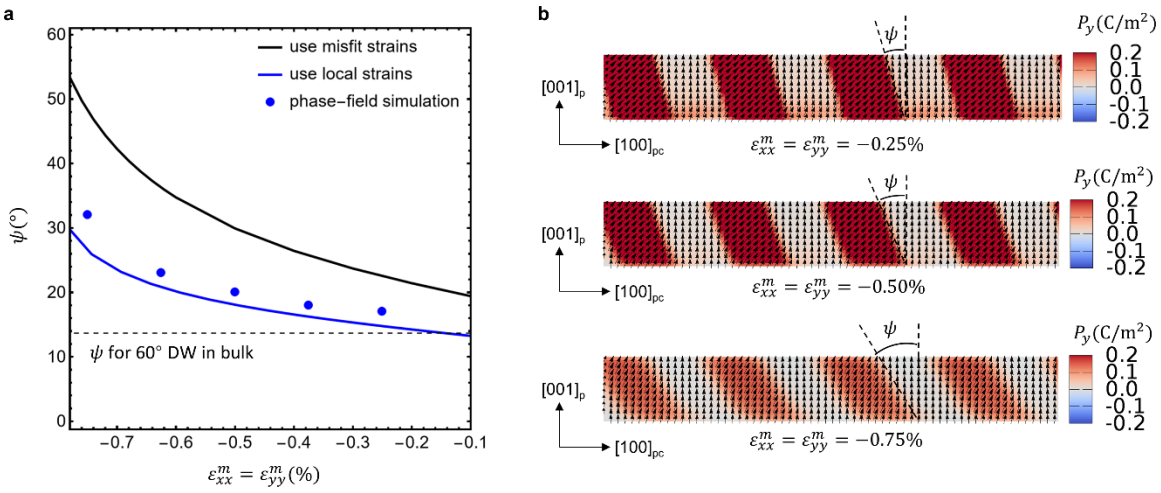

Figure 5 The effect of misfit strain on the domain wall orientation of a_1c/a_2c polydomain for $K_{0.7}Na_{0.3}NbO_3$ thin films. (a) The domain wall inclination angle ψ as a function of the biaxial misfit strain $\varepsilon_{xx}^m = \varepsilon_{yy}^m$ calculated by the microelasticity theory when using the local strains (blue curve) and the overall misfit strains (black curve). The black points are measured angle ψ from phase-field simulation results. (b) Cross section view of the polarization distribution in the $(010)_{pc}$ plane of the simulated polydomain structure subject to different biaxial misfit strains. The definition of the domain wall inclination angle ψ is denoted.

We take the a_1c/a_2c polydomain of as an example and determine the domain wall orientation as a function of the misfit strain by assuming equibiaxial compressive misfit strains ($\varepsilon_{xx}^m = \varepsilon_{yy}^m = -0.1\% \sim -0.8\%$). The calculated domain wall inclination angle ψ as a function of the compressive misfit strain is shown in Figure 5a while the angle ξ remains unchanged $\xi = 45°$. As a comparison, we also performed corresponding phase-field simulations and measured the domain wall angles ψ as shown in Figure 5b. Both the theory and simulation suggest that the domain wall becomes more slanted with respect to the $(110)_{pc}$ direction as the misfit strain becomes more compressive. The domain wall inclination predicted by the theory tends to be slightly lower than the phase-field simulation, which may result from the domain wall energy associated with the domain size effects in the phase-field simulations, which will be discussed in Section 3.3.3.

We also notice a correlation between the ratio of polarization vector components and the domain wall inclination angle, which can be established analytically as shown below. As the a_1c/a_2c polydomain consists of a_1c and a_2c domains that are equivalent by symmetry, their domain walls are permissible domain walls whose orientation can be derived from the mechanical compatibility condition. With a simple algebra we show that the permissible domain wall between the $a_1^+c^+$ and $a_2^+c^+$ domain variants is $(11k)_{pc}$ with

$$k = \frac{2Q_{44}}{Q_{11} - Q_{12}} \frac{P_{\mathrm{op}}}{P_{\mathrm{ip}}}, \tag{12}$$

where P_{ip} and P_{op} are the *in-plane* and *out-of-plane* polarization of the $a_1^+c^+$domain (same for the $a_2^+c^+$ domain). The domain wall inclination angle ψ is related to k by $\psi = \tan^{-1}(k)$. Therefore, the more monoclinic distortion of the lattice (measured by $\frac{P_{\mathrm{op}}}{P_{\mathrm{ip}}}$), the more tilted of the domain wall (ψ). Similar trends have also been suggested in the theoretical study of monoclinic relaxor-ferroelectric bulk crystals(28).

Notice that in some previous works, the strain states of coexisting domains are assumed to be the same as the overall misfit strains. In this sense, we have $\varepsilon_{xx}^{\alpha} = \varepsilon_{xx}^{m}$ and $\varepsilon_{yy}^{\alpha} = \varepsilon_{yy}^{m}$ for $\alpha = a_1^+c^+$ and $a_2^+c^+$. This assumption might not affect the domain wall plane when it has a fixed orientation as for the polydomain of tetragonal polydomain (e.g., 90° domain walls of *a*/*c* domains of $PbTiO_3$), but it will significantly influence the domain wall orientation for the monoclinic phase considered in this work. This point is demonstrated in the black line in Figure 5a where the overall misfit strain is used for the minimization of Equation (6).

3.3.2 Effect of electrostrictive coefficients

As suggested by Equation (12), the domain wall orientations of monoclinic polydomains depend on the value of the electrostrictive coefficients. However, there is a large discrepancy in the choice for Q_{44} of $K_{0.5}Na_{0.5}NbO_3$ in literature(23,24). Here, we show how the magnitude of Q_{44} can influence the predicted domain wall orientations for the two polydomain structures. The analytically predicted and phase-field simulated domain wall inclination angles ψ and ξ as a function of the chemical composition of KNN films are shown in Figure 6a and b, respectively, for the a_1c/a_2c and a_1a_2/M_C polydomain structures by assuming different values of the Q_{44}^{KNN}. To exclude the misfit strain effects, we fixed the values of the misfit strains and strains of individual

domain/phase for all the cases as labeled in Figure 6. By comparing with the domain wall inclination angles measured from experiments (labeled as green points in Figure 6), we find by using $Q_{44}^{\mathrm{KNN}} = 0.029\ \mathrm{m^4C^{-2}}$ the best agreement is achieved for the a_1c/a_2c polydomain while it is not straightforward to distinguish from the $a_1a_2/\mathrm{M_C}$ polydomain. Nevertheless, the trend that the angle ξ decreases with respect to the composition x for the $a_1a_2/\mathrm{M_C}$ polydomain agrees better when we use $Q_{44}^{\mathrm{KNN}} = 0.029\ \mathrm{m^4C^{-2}}$. In addition, we also estimated Q_{44}^{KNN} based on the lattice constants of bulk KNN at varied temperature(50) which gives $Q_{44}^{\mathrm{KNN}} = 0.028\ \mathrm{m^4C^{-2}}$. Therefore, we conclude that $Q_{44}^{\mathrm{KNN}} = 0.029\ \mathrm{m^4C^{-2}}$ among others is the most reliable choice and should be adopted in the future studies of KNN.

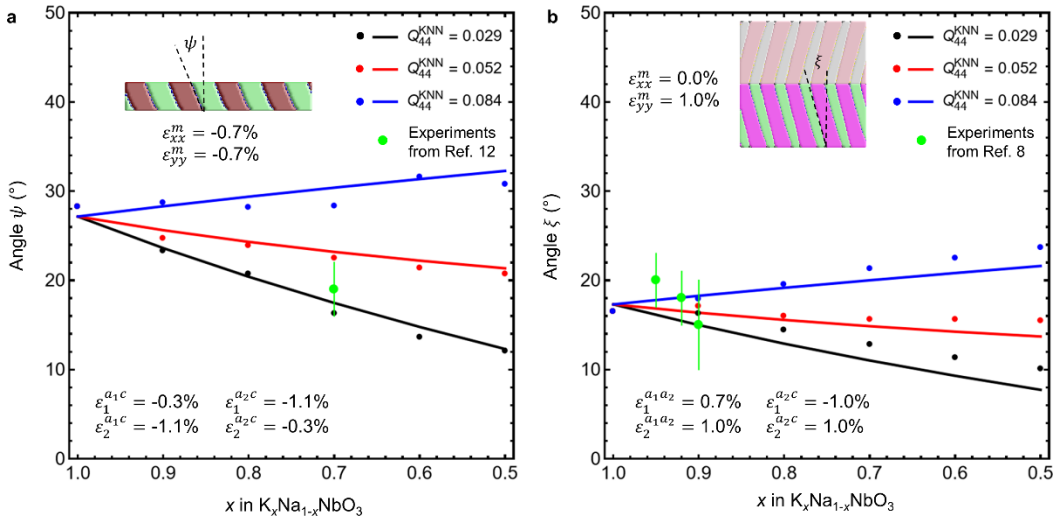

Figure 6 The effect of electrostrictive coefficients on domain wall orientations of the a_1c/a_2c and $a_1a_2/\mathrm{M_C}$ polydomain in $K_xNa_{1-x}NbO_3$ thin films with various composition x. (a) The domain wall inclination angle ψ as a function of x for the a_1c/a_2c polydomain subject to misfit strains $\varepsilon_{xx}^m = \varepsilon_{yy}^m = -0.7\%$. (b) The domain wall inclination angle ξ as a function of x for the $a_1a_2/\mathrm{M_C}$ polytwin domains subject to misfit strains $\varepsilon_{xx}^m = 0.0\%$ and $\varepsilon_{yy}^m = -0.7\%$. The insets in (a,b) schematically show the definition of angles ψ and ξ. The local strains of each domain are denoted explicitly. The

angles calculated by the microelasticity theory are plotted in lines while the angles measured from phase-field simulations are plotted by dots. The angles reported from experiments are labeled by green dots with error bars.

3.3.3 Effect of domain size

When predicting the domain wall orientation using the analytical strain phase equilibria theory described in Section 2.4, we do not include the domain wall energy contribution to the thermodynamics, and thus we ignore the finite size of the domains or the finite thickness of the films. However, the domain size is directly related to the film thickness as a result of the relaxation of elastic strain energy, which is self-consistently considered in the phase-field simulations. Therefore, we construct a series of polydomain structures in the phase-field model with different numbers of stripes while keeping the same film thickness (i.e., 20 nm) and relax the system to obtain the polydomain structure at equilibrium and the domain inclination angles ψ and ξ, as shown in Figure 8. We find that, in both cases, the domain walls become more slanted as the domain size increases, and a larger domain size dependence is seen for the $a_1^+c^+/a_2^+c^+$ polydomain. The domain size dependency suggested another tunability of the domain wall orientation by modulating the domain wall density of the monoclinic ferroelectric thin films.

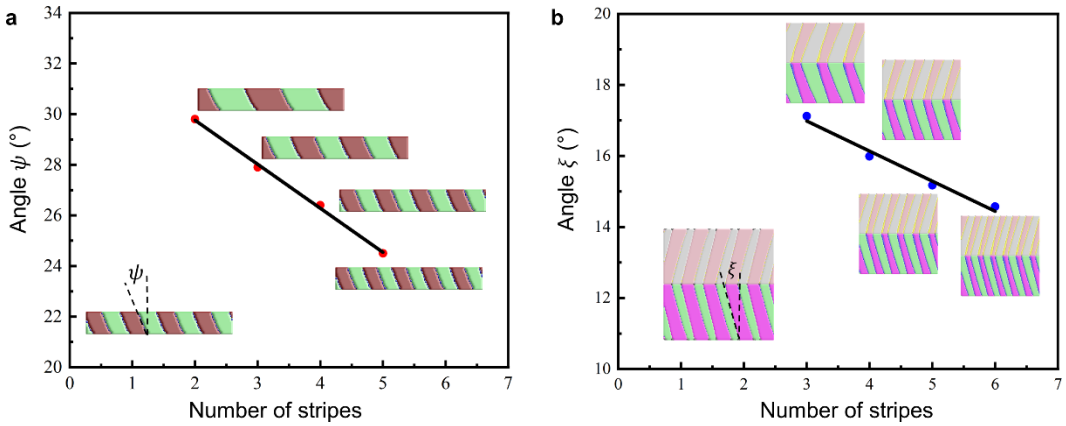

Figure 7 The effect of domain size on the domain wall orientation of the polydomain structures obtained by phase-field simulations. (a) The domain wall inclination angle ψ as a function of the domain wall density measured by the number of stripe patterns for the $a_1^+c^+/a_2^+c^+$ polydomain of $KNbO_3$ thin films with misfit strains $\varepsilon_{xx}^m = \varepsilon_{yy}^m = -0.5\%$. (b) The domain wall inclination angle ξ as a function of the domain wall density measured by the number of stripe patterns for the $a_1^+a_2^+/a_2^+c^+$ polydomain of $KNbO_3$ thin films with misfit strains $\varepsilon_{xx}^m = -0.2\%$ and $\varepsilon_{yy}^m = 1.0\%$. The insets in (a) are the section views along $(010)_{pc}$ of the simulated polydomain at equilibrium. The insets in (b) are the top views of the simulated polydomain at equilibrium. The definitions of the angles ψ and ξ are illustrated. The solid black lines in (a,b) are linear fits of the data points.

3.3.4 Influence of in-plane periodic boundary conditions

In the phase-field simulations of ferroelectric thin films, the in-plane periodic boundary condition is often assumed. It is compatible with stripe-like polydomain patterns when the domain wall planes are parallel to the *x* or *y* directions but may impose restriction on the domain wall motion when the domain wall plane tends to rotate along the out-of-plane direction. We demonstrate this scenario here because, without paying attention to this factor, it may lead to incorrect prediction of the domain wall behavior.

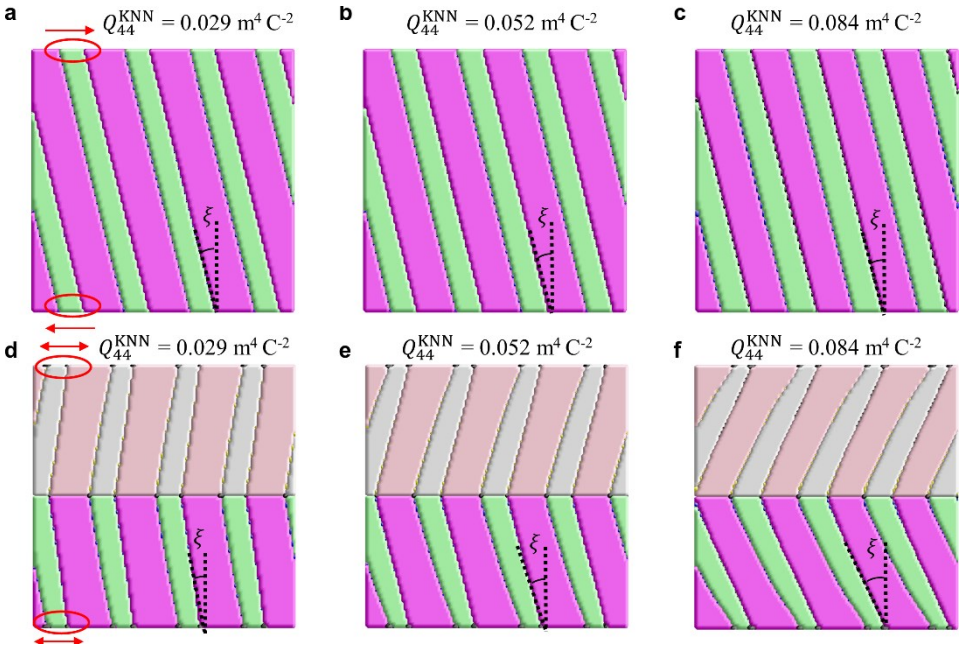

Figure 8 The influence of in-plane periodic boundary conditions adopted in the phase-field simulation on determination of domain wall orientation for the a_1a_2/M_C polydomain. (a,b,c) The single-bundle and (d,e,f) two-bundle of $a_1^+a_2^+/a_2^+c^+$ polydomain structures at equilibrium using different electrostrictive coefficient Q_{44}^{KNN} of $K_{0.5}Na_{0.5}NbO_3$. The misfit strains are kept at $\varepsilon_{xx}^m = -0.2\%$ and $\varepsilon_{yy}^m = 1.0\%$ for all the cases.

We take the $a_1^+a_2^+/a_2^+c^+$ polydomain for $K_{0.5}Na_{0.5}NbO_3$ thin films subject to $\varepsilon_{xx}^m = -0.2\%$ and $\varepsilon_{yy}^m = 1.0\%$ as an example. From the simulated polydomain structure at equilibrium as the initial state, we vary the value of Q_{44}^{KNN} from 0.029 to 0.084 m^4C^{-2} and relax the system. We find that the domain wall angle remains unchanged while the elastic strain energy of the system increases, suggesting that the relaxation by the domain wall motion is suppressed. This can be attributed to the restriction on the domain wall motion imposed by periodic boundary condition. For example, if the domain wall inclination angle ξ tends to increase, the junction of the domain walls at the upper boundary in Figure 8a tend to move left while the junction of the domain walls at the bottom tends to move right, as indicated by the red circles, which is not conformal. To overcome this

restriction, a simple way is to construct a pair of equivalent polydomain to form the double-bundle structure so the domain walls at the system boundaries can move consistently as angle ξ varies. In all the calculations shown above, we adopted the double-bundle structure for $a_1^+a_2^+/a_2^+c^+$ polydomain to avoid this artifact. For $a_1^+c/a_2^+c^+$ polydomains, there is no such issue because angle ξ keeps at $\xi = 45°$ in all cases due to symmetry requirements.

4. Summary and Perspective

We demonstrate an analytical strain phase equilibria theory for establishing the strain phase diagrams and predicting the domain wall orientations of two types of polydomain of $(001)_{pc}$-oriented monoclinic KNN thin films. We show that the analytical predictions from the strain phase equilibria theory on the formation of polydomain structures and domain wall orientations are not only largely consistent with the results from more realistic but much more computationally expensive three-dimensional phase-field simulations but also in good agreement with existing experimental measurements. The fact that these agreements have been achieved for KNN thin films with various compositions and misfit strain states suggest a general applicability and effectiveness of the analytical strain phase equilibria theory. We expect the demonstrated success of the theoretical framework can lead to its further extension to understand and predict the strain phase equilibria and domain walls in emerging ferroelectric materials such as HfO_2 (58).

Aside from the demonstrated theoretical approach, our work also helps gain fundamental insights into the domain structure of monoclinic KNN. KNN-based ceramics have been shown excellent electromechanical properties comparable to that of $Pb(Zr_{1-x}Ti_x)O_3$ (PZT) and thus been regarded as a promising lead-free alternative to PZT for piezoelectric applications (59). It remains an open question whether these excellent functional properties can be retained into thin films. Therefore, it would be of great interest to further establish the relationship between the domain structure and

the piezoelectric and dielectric properties of KNN-based thin films(22) which will be of both scientific interest and technological relevance.

We shall point out that, in this work, we only focus on two polydomain structures of the monoclinic M_C phase where the difference between the polarization vectors of the neighboring domains is small, i.e., corresponding to the 60° domain walls of the undistorted bulk orthorhombic phase. There are many other types of polydomain combinations, such as the $a_1^+c^+$ and $a_2^+c^-$ which corresponds to the 120° domain walls of the bulk orthorhombic counterpart, and possible charged domain walls where the electrostatic energy may dominate the domain wall orientations. A comprehensive theoretical investigation of all possible low-energy domain walls of M_C-phase ferroelectrics will require significant future efforts.

Acknowledgment

B.W. and L.-Q.C. acknowledge support by the National Science Foundation (NSF) through Grant No. DMR- 2133373. Part of this work was performed under the auspices of the U.S. Department of Energy by Lawrence Livermore National Laboratory under Contract DE-AC52-07NA27344 (B.W.). A.L. acknowledges funding from the Materials Research Science and Engineering Center (MRSEC) of The Pennsylvania State University, supported by the NSF under Grant. No. DMR-1420620 and DMR-2011839. The computer simulations were performed using the commercial software package μ-PRO (http://mupro.co/contact/) on the ICS-ACI Computing Systems at Pennsylvania State University and at the Extreme Science and Engineering Discovery Environment cluster, which used the Comet system at the UC San Diego. B.W. is thankful to Dr. Laura Bogula, Dr. Martin Schmidbauer and Dr. Jutta Schwarzkopf for fruitful discussions.

Rerferences

1. Shkuratov SI, Lynch CS. A review of ferroelectric materials for high power devices. J Materiomics. 2022 Jul 1;8(4):739–52.
2. Zhang S, Li F, Jiang X, Kim J, Luo J, Geng X. Advantages and challenges of relaxor-PbTiO3 ferroelectric crystals for electroacoustic transducers – A review. Prog Mater Sci. 2015 Mar;68:1–66.
3. Scott JF, Araujo CAPD. Ferroelectric Memories. Sci New Ser. 1989;246(4936):1400–5.
4. Wessels BW. Ferroelectric Epitaxial Thin Films for Integrated Optics. Annu Rev Mater Res. 2007 Aug 1;37(1):659–79.
5. Streiffer SK, Parker CB, Romanov AE, Lefevre MJ, Zhao L, Speck JS, et al. Domain patterns in epitaxial rhombohedral ferroelectric films. I. Geometry and experiments. J Appl Phys. 1998 Mar 1;83(5):2742–53.
6. Speck JS, Daykin AC, Seifert A, Romanov AE, Pompe W. Domain configurations due to multiple misfit relaxation mechanisms in epitaxial ferroelectric thin films. III. Interfacial defects and domain misorientations. J Appl Phys. 1995 Aug;78(3):1696–706.
7. Fousek J, Janovec V. The Orientation of Domain Walls in Twinned Ferroelectric Crystals. J Appl Phys. 1969 Jan;40(1):135–42.
8. Braun D, Schmidbauer M, Hanke M, Kwasniewski A, Schwarzkopf J. Tunable ferroelectric domain wall alignment in strained monoclinic $K_x Na_{1-x} NbO_3$ epitaxial films. Appl Phys Lett. 2017 Jun 5;110(23):232903.
9. Luo J, Sun W, Zhou Z, Lee HY, Wang K, Zhu F, et al. Monoclinic (K,Na)NbO_3 Ferroelectric Phase in Epitaxial Films. Adv Electron Mater. 2017 Oct;3(10):1700226.
10. Luo J, Sun W, Zhou Z, Bai Y, Wang ZJ, Tian G, et al. Domain Evolution and Piezoelectric Response across Thermotropic Phase Boundary in (K,Na)NbO_3 -Based Epitaxial Thin Films. ACS Appl Mater Interfaces. 2017 Apr 19;9(15):13315–22.
11. Braun D, Schmidbauer M, Hanke M, Schwarzkopf J. Hierarchy and scaling behavior of multi-rank domain patterns in ferroelectric K0.9Na0.1NbO3 strained films. Nanotechnology. 2017 Nov;29(1):015701.
12. von Helden L von, Schmidbauer M, Liang S, Hanke M, Wördenweber R, Schwarzkopf J. Ferroelectric monoclinic phases in strained K0.70Na0.30NbO3 thin films promoting selective surface acoustic wave propagation. Nanotechnology. 2018 Aug;29(41):415704.
13. von Helden L, Bogula L, Janolin PE, Hanke M, Breuer T, Schmidbauer M, et al. Huge impact of compressive strain on phase transition temperatures in epitaxial ferroelectric KxNa1−xNbO3 thin films. Appl Phys Lett. 2019 Jun 13;114(23):232905.
14. Bogula L, Von Helden L, Richter C, Hanke M, Schwarzkopf J, Schmidbauer M. Ferroelectric phase transitions in multi-domain $K_{0.9} Na_{0.1} NbO_3$ epitaxial thin films. Nano Futur. 2020 Aug 4;4(3):035005.
15. Schmidbauer M, Braun D, Markurt T, Hanke M, Schwarzkopf J. Strain engineering of monoclinic domains in $K_x Na_{1-x} NbO_3$ epitaxial layers: a pathway to enhanced piezoelectric properties. Nanotechnology. 2017 Jun 16;28(24):24LT02.
16. Schmidbauer M, Bogula L, Wang B, Hanke M, von Helden L, Ladera A, et al. Temperature dependence of three-dimensional domain wall arrangement in ferroelectric K0. 9Na0. 1NbO3 epitaxial thin films. J Appl Phys. 2020;128(18):184101.
17. Schwarzkopf J, Braun D, Hanke M, Uecker R, Schmidbauer M. Strain Engineering of Ferroelectric Domains in KxNa1−xNbO3 Epitaxial Layers. Front Mater. 2017 Aug 16;4:26.
18. Wang Y, Bin Anooz S, Niu G, Schmidbauer M, Wang L, Ren W, et al. Thickness effect on ferroelectric domain formation in compressively strained K 0.65 Na 0.35 NbO 3 epitaxial films. Phys Rev Mater. 2022 Aug 31;6(8):084413.
19. Luo J, Liu L, Zhang SW, Li JF. Ferroelectric Domain Structures in Monoclinic (K0.5Na0.5)NbO3 Epitaxial Thin Films. Phys Status Solidi RRL – Rapid Res Lett. 2021;15(6):2100127.

20. Schwarzkopf J, Braun D, Hanke M, Kwasniewski A, Sellmann J, Schmidbauer M. Monoclinic MA domains in anisotropically strained ferroelectric K0.75Na0.25NbO3 films on (110) TbScO3 grown by MOCVD. J Appl Crystallogr. 2016 Apr 1;49(2):375–84.
21. Zhou MJ, Wang B, Ladera A, Bogula L, Liu HX, Chen LQ, et al. Phase diagrams, superdomains, and superdomain walls in KxNa1-xNbO3 epitaxial thin films. Acta Mater. 2021;215:117038.
22. Zhou MJ, Wang B, Peng K, Liu HX, Chen LQ, Nan CW. Phase-field simulation of domain size effect on dielectric and piezoelectric responses in K0.5Na0.5NbO3 epitaxial thin films with superdomain structures. Acta Mater. 2023 Apr 15;248:118777.
23. Zhou MJ, Wang JJ, Chen LQ, Nan CW. Strain, temperature, and electric-field effects on the phase transition and piezoelectric responses of K0.5Na0.5NbO3 thin films. J Appl Phys. 2018 Apr 20;123(15):154106.
24. Wang B, Chen HN, Wang JJ, Chen LQ. Ferroelectric domain structures and temperature-misfit strain phase diagrams of K1-xNaxNbO3 thin films: A phase-field study. Appl Phys Lett. 2019;115(9):092902.
25. Xue F, Ji Y, Chen LQ. Theory of strain phase separation and strain spinodal: Applications to ferroelastic and ferroelectric systems. Acta Mater. 2017 Jul 1;133:147–59.
26. Xue F, Li Y, Gu Y, Zhang J, Chen LQ. Strain phase separation: Formation of ferroelastic domain structures. Phys Rev B. 2016 Dec 2;94(22):220101.
27. Wang B, Chen LQ. Theory of Strain Phase Equilibria and Diagrams. SSRN; 2024.
28. Bokov AA, Ye ZG. Domain structure in the monoclinic Pm phase of Pb(Mg1/3Nb2/3)O3–PbTiO3 single crystals. J Appl Phys. 2004 May 25;95(11):6347–59.
29. Biran I, Gorfman S. Permissible domain walls in monoclinic MAB ferroelectric phases. Acta Crystallogr Sect Found Adv. 2024 Jan 1;80(1).
30. Sapriel J. Domain-wall orientations in ferroelastics. Phys Rev B. 1975 Dec 1;12(11):5128–40.
31. Erhart J. Domain wall orientations in ferroelastics and ferroelectrics. Phase Transit. 2004;77(12):989–1074.
32. Mantri S, Daniels J. Domain walls in ferroelectrics. J Am Ceram Soc. 2021;104(4):1619–32.
33. Ouyang J, Zhang W, Huang X, Roytburd AL. Thermodynamics of formation of tetragonal and rhombohedral heterophase polydomains in epitaxial ferroelectric thin films. Acta Mater. 2011 Jun;59(10):3779–91.
34. Zhang Y, Xue F, Wang B, Hu JM, Dong S, Liu JM, et al. Stability and low-energy orientations of interphase boundaries in multiaxial ferroelectrics: Phase-field simulations. Phys Rev B. 2022;105(1):014108.
35. Roytburd AL, Ouyang J, Artemev A. Polydomain structures in ferroelectric and ferroelastic epitaxial films. J Phys Condens Matter. 2017 Mar;29(16):163001.
36. Vailionis A, Boschker H, Siemons W, Houwman EP, Blank DHA, Rijnders G, et al. Misfit strain accommodation in epitaxial A B O 3 perovskites: Lattice rotations and lattice modulations. Phys Rev B. 2011 Feb 11;83(6):064101.
37. Janolin PE. Strain on ferroelectric thin films: Example of Pb(Zr1−xTix)O3. J Mater Sci. 2009 Oct;44(19):5025–48.
38. Pohlmann H, Wang JJ, Wang B, Chen LQ. A thermodynamic potential and the temperature-composition phase diagram for single-crystalline K1-x Na x NbO3 ($0 \leq x \leq 0.5$). Appl Phys Lett. 2017;110(10):102906.
39. Hillert M. Phase Equilibria, Phase Diagrams and Phase Transformations: Their Thermodynamic Basis. Cambridge University Press; 2007.
40. Bednyakov PS, Sturman BI, Sluka T, Tagantsev AK, Yudin PV. Physics and applications of charged domain walls. Npj Comput Mater. 2018 Dec;4(1):65.
41. Xue F, Gu Y, Liang L, Wang Y, Chen LQ. Orientations of low-energy domain walls in perovskites with oxygen octahedral tilts. Phys Rev B. 2014 Dec 1;90(22):220101.
42. Khachaturyan AG. Theory of structural transformations in solids. Courier Corporation; 2013.

43. Cheng H, Ouyang J, Zhang YX, Ascienzo D, Li Y, Zhao YY, et al. Demonstration of ultra-high recyclable energy densities in domain-engineered ferroelectric films. Nat Commun. 2017 Dec;8(1):1999.
44. Chen LQ. Phase-Field Method of Phase Transitions/Domain Structures in Ferroelectric Thin Films: A Review. J Am Ceram Soc. 2008;91(6):1835–44.
45. Wang JJ, Wang B, Chen LQ. Understanding, predicting, and designing ferroelectric domain structures and switching guided by the phase-field method. Annu Rev Mater Res. 2019;49:127–52.
46. Li YL, Hu SY, Liu ZK, Chen LQ. Effect of substrate constraint on the stability and evolution of ferroelectric domain structures in thin films. Acta Mater. 2002 Jan 22;50(2):395–411.
47. Li YL, Hu SY, Liu ZK, Chen LQ. Effect of electrical boundary conditions on ferroelectric domain structures in thin films. Appl Phys Lett. 2002 Jul 15;81(3):427–9.
48. Liang L, Li YL, Chen LQ, Hu SY, Lu GH. Thermodynamics and ferroelectric properties of KNbO3. J Appl Phys. 2009 Nov 15;106(10):104118.
49. Skjærvø SL, Høydalsvik K, Blichfeld AB, Einarsrud MA, Grande T. Thermal evolution of the crystal structure and phase transitions of KNbO3. R Soc Open Sci. 2018 Jun 20;5(6):180368.
50. Pop-Ghe P, Stock N, Quandt E. Suppression of abnormal grain growth in K0.5Na0.5NbO3: phase transitions and compatibility. Sci Rep. 2019 Dec 24;9(1):19775.
51. Orayech B, Faik A, López GA, Fabelo O, Igartua JM. Mode-crystallography analysis of the crystal structures and the low- and high-temperature phase transitions in $Na_{0.5}K_{0.5}NbO_3$. J Appl Crystallogr. 2015 Apr 1;48(2):318–33.
52. Hirschle C, Schreuer J, Ganschow S, Peters L. Thermoelastic anisotropy in NdScO3 and NdGaO3 perovskites. Mater Chem Phys. 2020 Nov 1;254:123528.
53. Hirschle C, Schreuer J, Ganschow S, Schulze-Jonack I. Thermoelastic properties of rare-earth scandates SmScO3, TbScO3 and DyScO3. J Appl Phys. 2019 Oct 23;126(16):165103.
54. Uecker R, Velickov B, Klimm D, Bertram R, Bernhagen M, Rabe M, et al. Properties of rare-earth scandate single crystals (Re=Nd−Dy). J Cryst Growth. 2008 May;310(10):2649–58.
55. Giencke JE, Folkman CM, Baek SH, Eom CB. Tailoring the domain structure of epitaxial BiFeO3 thin films. Curr Opin Solid State Mater Sci. 2014 Feb 1;18(1):39–45.
56. Lee J, Eom K, Paudel T, Wang B, Lu H, Huyan H, et al. In-plane quasi-single-domain BaTiO3 via interfacial symmetry engineering. Nat Commun. 2021;12(1):1–8.
57. Chen ZH, Damodaran AR, Xu R, Lee S, Martin LW. Effect of "symmetry mismatch" on the domain structure of rhombohedral BiFeO3 thin films. Appl Phys Lett. 2014 May 8;104(18):182908.
58. Schroeder U, Park MH, Mikolajick T, Hwang CS. The fundamentals and applications of ferroelectric HfO2. Nat Rev Mater. 2022 Aug;7(8):653–69.
59. Li JF, Wang K, Zhang BP, Zhang LM. Ferroelectric and Piezoelectric Properties of Fine-Grained Na0.5K0.5NbO3 Lead-Free Piezoelectric Ceramics Prepared by Spark Plasma Sintering. J Am Ceram Soc. 2006 Feb;89(2):706–9.

Table 1. Materials coefficients used for $K_{1-x}Na_xNbO_3$ ($0 \le x \le 0.5$) in the Landau-type model and phase-field simulations in this work.

Parameters	Units	Values (Ref.(38))	Parameters	Units	Values (Ref.(24))
α_1	C^{-2} m^2 N	$2x \times 4.29 \times 10^7 \times \left[\coth\left(\frac{140}{T}\right) - \coth\left(\frac{140}{657}\right)\right] + (1-2x) \times 5.98 \times 10^7 \times \left[\coth\left(\frac{140}{T}\right) - \coth\left(\frac{140}{650}\right)\right]$	c_{11}	GPa	230
α_{11}	C^{-4} m^6 N	$2x \times (-2.7302 \times 10^8) + (1-2x) \times (-6.36 \times 10^8)$	c_{12}	GPa	90
α_{12}	C^{-4} m^6 N	$2x \times (1.0861 \times 10^9) + (1-2x) \times (9.66 \times 10^8)$	c_{44}	GPa	76
α_{111}	C^{-6} m^{10} N	$2x \times (3.0448 \times 10^9) + (1-2x) \times (2.81 \times 10^9)$	Q_{11}	m^4/C^2	$2x \times 0.166 + (1-2x) \times 0.13$
α_{112}	C^{-6} m^{10} N	$2x \times (-2.7270 \times 10^9) + (1-2x) \times (-1.99 \times 10^9)$	Q_{12}	m^4/C^2	$2x \times (-0.072) + (1-2x) \times (-0.047)$
α_{123}	C^{-6} m^{10} N	$2x \times (1.5513 \times 10^{10}) + (1-2x) \times (4.50 \times 10^9)$	Q_{44}	m^4/C^2	$2x \times Q_{44}^{\mathrm{KNN}} + (1-2x) \times 0.052$
α_{1111}	C^{-8} m^{14} N	$2x \times (2.4044 \times 10^{10}) + (1-2x) \times (1.74 \times 10^{10})$	Q_{44}^{KNN}	m^4/C^2	0.029, or 0.052, or 0.084[a]

α_{1112}	$C^{-8}m^{14}N$	$2x \times (3.7328 \times 10^9) + (1 - 2x) \times (5.99 \times 10^9)$	g_{11}	N/m^4C^2	0.64×10^{-11}
α_{1122}	$C^{-8}m^{14}N$	$2x \times (3.3485 \times 10^{10}) + (1 - 2x) \times (2.5 \times 10^{10})$	g_{12}	N/m^4C^2	-0.64×10^{-11}
α_{1123}	$C^{-8}m^{14}N$	$2x \times (-6.2017 \times 10^{10}) + (1 - 2x) \times (-1.17 \times 10^{10})$	g_{44}	N/m^4C^2	0.64×10^{-11}

[a] Various values are used for the Q_{44} of $K_{0.5}Na_{0.5}NbO_3$ in the literature (23,24); Based on our results, it is more accurate to use 0.029 m^4/C^2 among others.

Table 2. Calculated misfit strains for $K_xNa_{1-x}NbO_3$ epitaxial thin films grown on various substrate materials

x of $K_xNa_{1-x}NbO_3$	Substrate materials	ε_{xx}^{m}	ε_{yy}^{m}	ε_{avg}^{m}	Expt. reported phases	Theoretical predicted phases
0.9	$NdScO_3$	0.06%	0.37%	0.21%	a_1a_2/M_C	a_1a_2/M_C[*]
	$SmScO_3$	-0.16%	0.08%	-0.04%	a_1c/a_2c	a_1c/a_2c
	$GdScO_3$	-0.54%	-0.44%	-0.49%	a_1c/a_2c	a_1c/a_2c
0.7[b]	$TbScO_3$	-0.72%	-0.66%	-0.69%	a_1c/a_2c	a_1c/a_2c
	$DyScO_3$	-0.91%	-1.04%	-0.98%	c	c
0.5[c]	$SrTiO_3$	-1.82% (-0.71%)[d]	-1.82% (-0.71%)[d]	-1.82% (-0.71%)	a_1c/a_2c	a_1c/a_2c

[a] With stronger anisotropy of the misfit strains as discussed in the text.

[b] The x ranges from 0.54 ~ 0.77 in Ref. (8); x = 0.7 is used here for convenience.

[c] The composition is $Li_{0.06}K_{0.47}Na_{0.47}NbO_3$ in Ref. (10). x = 0.5 is used here for convenience.

[d] The relaxed misfit strains calculated using the experiment measured lattice constants of the films.